ACS APPLIED MATERIALS & INTERFACES

www.acsami.org

Research Article

Metal-Free, Graphene Oxide-Based Tunable Soliton and Plasmon Engineering for Biosensing Applications

Seemesh Bhaskar, Naga Sai Visweswar Kambhampati, K. M. Ganesh, Mahesh Sharma P, Venkatesh Srinivasan,* and Sai Sathish Ramamurthy*

Cite This: *ACS Appl. Mater. Interfaces* 2021, 13, 17046−17061

Read Online

ACCESS | Metrics & More | Article Recommendations | Supporting Information

ABSTRACT: The quest for auxiliary plasmonic materials with lossless properties began in the past decade. In the current study, a unique plasmonic response is demonstrated from a stratified high refractive index (HRI)−graphene oxide (GO) and low refractive index (LRI)−polymethyl methacrylate (PMMA) multistack. Graphene oxide plasmon-coupled emission (GraPE) reveals the existence of strong surface states on the terminating layer of the photonic crystal (PC) framework. The chemical defects in GO thin film are conducive for unraveling plasmon hybridization within and across the multistack. We have achieved a unique assortment of metal-dielectric-metal (MDM) ensuing a zero-normal steering emission on account of solitons as well as directional GraPE. This has been theoretically established and experimentally demonstrated with a metal-free design. The angle-dependent reflectivity plots, electric field energy (EFI) profiles, and finite-difference time-domain (FDTD) analysis from the simulations strongly support plasmonic modes with giant Purcell factors (PFs). The architecture presented prospects for the replacement of metal-dependent MDM and surface plasmon-coupled emission (SPCE) technology with low cost, easy to fabricate, tunable soliton [graphene oxide plasmon-coupled soliton emission (GraSE)], and plasmon [GraPE] engineering for diverse biosensing applications. The superiority of the GraPE platform for achieving 1.95 pg mL^{-1} limit of detection of human IFN-γ is validated experimentally. A variety of nanoparticles encompassing metals, intermetallics, rare-earth, and low-dimensional carbon−plasmonic hybrids were used to comprehend PF and cavity hot-spot contribution resulting in 900-fold fluorescence emission enhancements on a lossless substrate, thereby opening the door to unique light−matter interactions for next-gen plasmonic and biomedical technologies.

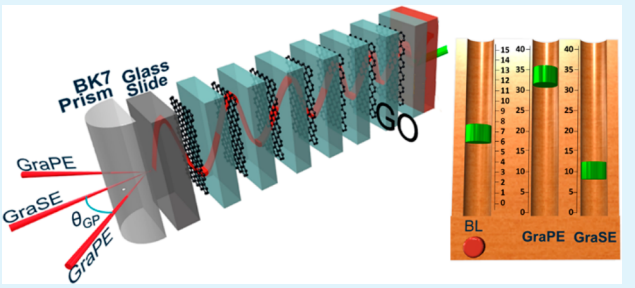

KEYWORDS: *graphene oxide plasmon-coupled emission, graphene oxide plasmon-coupled soliton emission, surface plasmon-coupled emission, nanointerface, Purcell factor, human IFN-γ biosensor*

INTRODUCTION

Applied nanoscience and plasmonics have prompted significant attention in the recent past on account of their tunable light−matter interactions, resulting in economical and industrial applications.[1] Frontier areas of research at interfaces in nano-optics and nanophotonics involve electromagnetic (EM) field trapping, control, tuning, evaluation, and manipulation, resulting in unearthing phenomena such as metal-dependent plasmonics,[2] dielectric-dependent metamaterials,[3] graphene-based plasmonics,[4] and photonic crystals (PCs).[5] Despite the versatility of metallic or metal-dielectric hybrid plasmons, their intrinsic dissipative Ohmic losses prevent the realization of theoretically established luminescence emission enhancements.[6] In this regard, several hybrid approaches combining PCs and graphene π-plasmons with metal-plasmons in a 3D interfacial multistack format vis-à-vis flatland nanophotonics have evolved with numerous benefits.[7]

Charge density perturbations on a variety of nanometal and hybrid graphene frameworks are studied and their multi-disciplinary applications have been reported.[8] A strong dependence of graphene plasmons on its Fermi energy has been used for tuning its optical properties by chemical doping and electrostatic gating. Further, the nonlinear properties of graphene and analogous 2D materials have dramatically influenced the understanding of traditional plasmonic concepts, with innovative breakthroughs on account of peculiarities of massless Dirac Fermions.[9] While the physical, electronic, and chemical properties of graphitic materials are being exploited with new insights, nanoplasmonic and photonic assessments are still in their nascent stage. In this context, the coupling of graphene plasmons with incident EM

Received: January 16, 2021
Accepted: March 22, 2021
Published: March 31, 2021

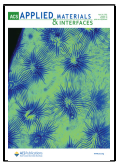

https://doi.org/10.1021/acsami.1c01024
ACS Appl. Mater. Interfaces 2021, 13, 17046−17061

radiation is indeed challenging.[10] However, in-plane momentum matching has been realized with nanoribbon or disk arrays,[11] graphene-dielectric-graphene nonlinear structure,[12,13] and spatial solitons-surface plasmon polaritons (SPPs) coupling.[14−16] Of late, multilayer graphene structures are being scrutinized to comprehend their linear and nonlinear contributions in altering coupling efficiency with incident EM radiation.[14−18] High conductivity induced strong quenching of quantum emitters in the vicinity of graphene sheets seems to contradict its intrinsic nature while taken in doped form presenting extreme EM-field confinement.[4] Conceivably, it would be more exciting to comprehend the effect of disjoint π-plasmons[13] (taken in a stacked format) on the performance of quantum emitters in terms of Purcell factors (PFs), quantum efficiency, and radiative and nonradiative decay lifetime. Several strategies are developed for the synthesis of graphene[19] from carbon-based materials that include chemical vapor deposition (CVD) and mechanical and solution exfoliation. However, graphene-dependent applications suffer from cost, time-effective mass-production, solubility, process ability, and flexibility in manufacturing procedures. As a result, graphene oxide (GO) has emerged as an essential analogue of graphene presenting equally robust characteristics.[20] Although single layer graphene oxide (SLGO) and exfoliated graphene layers were adopted in a surface plasmon-coupled emission (SPCE) platform, a metal-free and a template-free graphene oxide plasmon-coupled emission (GraPE) has not been reported hitherto. In this context, here, we report a key step toward π-plasmon-soliton substrate engineering by tailoring the solitons (nonlinear part) and plasmons (linear part) supported using a GO|PMMA multistack. Different methods such as CVD, magnetron sputtering, and polymerization are available for the fabrication of one-dimensional photonic crystals (1DPCs).[21] Nevertheless, innovative protocols are of great necessity to avoid complex fabrication strategies, making them amenable to studies in resource-limited settings (low- and middle-income countries). We have hence utilized spin-coating as a modest technique in this substrate design.[22]

By and large, our efforts have been to reproduce or mimic the capabilities of metal-dielectric interfaces with a GO-based PC framework. Our work helps rationalize the better output realized using this self-designed protocol in comparison with metal-dependent SPCE. Initial reports on Bragg-grating coupled emission (BGCE) specifies the observation of directional emission from 1DPCs on account of Bloch surface waves (BSWs) and internal optical modes (IOMs).[23] When 1DPC is coupled to a metal thin film (mimicking two adjacent 1DPCs), zero-degree normal emission Tamm states[24] have been observed. Likewise, metal-dielectric-metal (MDM) architectures in SPCE provide steering emission on account of coupling between cavity modes and SPP modes.[25] On the contrary, graphene multistacks are shown to support solitons[14−17] that are equivalent of Tamm states.[24,26,27] The first and only report[28] on graphene-based PC involved an alternating HRI and LRI framework, adopted to realize a significant resonance dip in the reflectance profile. In this report,[28] the reflectivity (resonance dips) is studied in a narrow range of angles (65°−80°). In the current study, we describe the use of SPCE,[29,30] a versatile platform to comprehend multiple dips in the reflectance profile, over the complete angular range starting from 0° to 90° with relevant theoretical and experimental elucidations. In this purview, the first-time use of a metal-free architecture has resulted in synergistic fluorescence enhancements with the use of the GO|PMMA multistack, discerning distinct properties on the basis of a combination of 'graphene oxide plasmon-coupled soliton emission' (abbreviated as GraSE) with steering[25] emission characteristic as well as 'graphene oxide plasmon-coupled emission' (abbreviated as GraPE) with directional property.[29] Since we were able to capture both beaming GraSE and directional GraPE in a single platform, we have termed the entire framework as the GraSP emission platform (a combination of GraSE and GraPE).

A methodical and successful demonstration of simulations and experimental results using the GraPE platform has been outlined, with an observation of 35-fold fluorescence emission enhancements. While metal-dependent SPCE showed ∼10-fold emission enhancements,[29,30] GraPE on account of its lossless[4,6,8] and nonlinear characteristics[15−17,31] provides augmented enhancements. The underlying near-field plasmon−plasmon interactions between the three-dimensionally stacked GO sheets presenting hybridized states are also detailed.[12−14] While terahertz[32] and IR range[33] tunable plasmonic response from graphene has been studied extensively, its response in the visible range is seldom reported. The study also presents the necessity and importance of adopting GO instead of graphene with concepts such as plasmon−plasmon hybridization, hole transport, and defects with cross-verification from high-resolution transmission electron microscopy (HRTEM), selected area electron diffraction (SAED), atomic force microscopy (AFM), and Raman studies. Further, cavity nanointerfaces supporting hot-spots of tunable intensities are elaborately discussed with four classes of chosen nanoparticles (NPs): (a) metals [Ag, Au, Pt] NPs, (b) intermetallics [SiO_2, TiO_2, TiC, TiN, TiCN], (c) rare-earth [Nd_2O_3] NPs, and (d) low-dimensional carbon substrate−metal plasmonic hybrids [CDs, AgCDs]. We attained an unprecedented 900-fold emission enhancements with the usage of AgCDs in GraPE on account of multifold hot-spots, presenting remarkable capabilities in hot-spot engineering in the presented micronano-interface. A label-free sandwich immunoassay is established for detection of human γ-interferon (HuIFN-γ) using a GraSP biosensor. The importance and relevance of detecting this antigen is comprehensively captured. The extreme EM-field entrapment between the plasmonic NP (linked to secondary antibody) and the Ag thin film (in case of SPCE) as well as the GO|PMMA multistack (in case of GraSP) assisted in enhancing the limit of detection of analytes. A comparative analysis between these results and that from conventional absorbance-based immunoassay and SPCE is given in detail. We anticipate an immediate deployment of the proposed GraSP engineering technology in bioanalytical sensing and point-of-care device applications.

The Results and Discussion section has been divided into five subsections broadly discussing the novel synthesis and characterization, which is followed by theoretical and experimental results with associated discussions and applications. First, all the details pertaining to validate the fabrication protocol developed are presented in Multistack Fabrication and Characterizations section. The second section titled Graphene Oxide Plasmon-Coupled Emission (GraPE) Analysis details all the theoretical and experimental analysis associated with the directional emission characteristic response of the fabricated multistack. This is followed by a third section titled Graphene Oxide Plasmon-Coupled Soliton Emission (GraSE) Analysis, describing the steering emission property of

https://doi.org/10.1021/acsami.1c01024
ACS Appl. Mater. Interfaces 2021, 13, 17046−17061

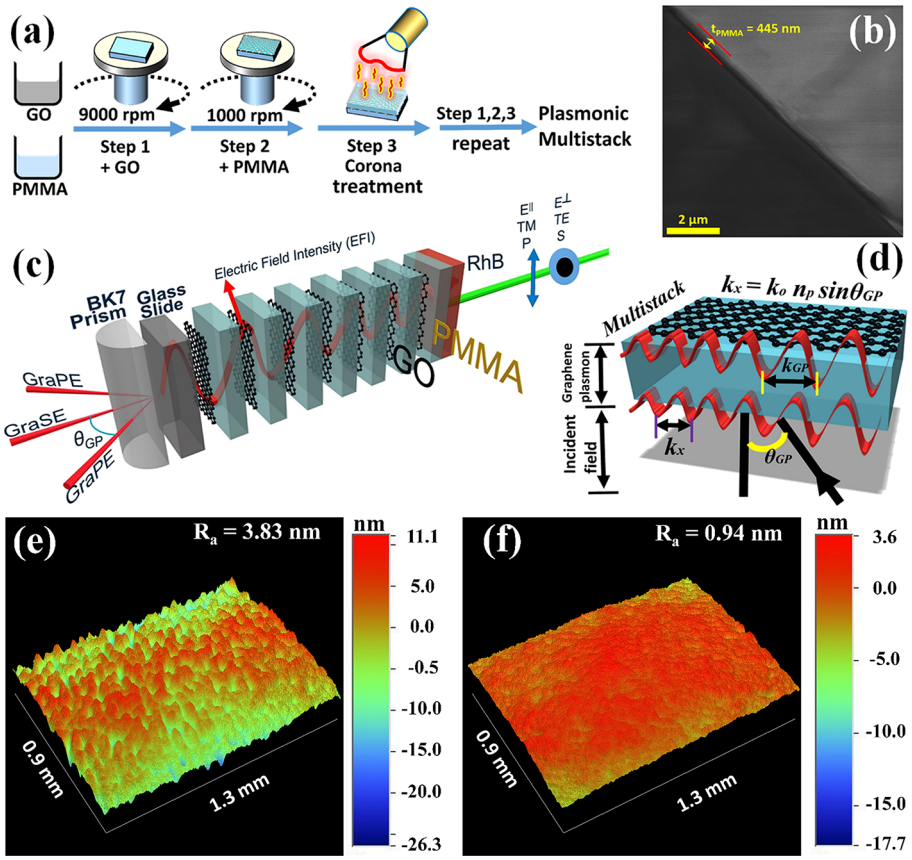

Figure 1. Fabrication of GO|PMMA multistack. (a) Schematic of fabrication protocol for obtaining GO|PMMA multistack. (b) Field emission scanning electron microscopy (FESEM) image of PMMA thin film. (c) Reverse Kretschmann (RK) configuration adopted in experimentation. The directional (at higher angle) and steering/beaming (at 0°) is highlighted in red. (d) Wave vector momentum phase matching of the incident radiation (k_x) with that of the multistack (k_{GP}). (e and f) Surface roughness measurements of PMMA thin film before and after corona treatment, respectively.

the fabricated multistack, where the experimental results are strongly supported by theoretical analysis. After we have demonstrated and validated the photonic response of the fabricated multistack in the first three sections (using theoretical and experimental details), we have presented the utility of these novel substrates in the perspective of broad applications for photonics and biosciences in the last two sections. That is, the penultimate section titled Metal, Intermetallic, Rare-Earth, and Carbon−Metal Hybrid NPs for Cavity Hot-Spot Generation demonstrates the utility of the multistack for obtaining tunable fluorescence enhancements where we have drawn logical and comparative conclusions with regard to the well-established SPCE platform. Finally, the last section Biosensing Applications of GraSP Emission Platform portrays the performance and functional efficacy of the multistack for sensing applications.

RESULTS AND DISCUSSION

Multistack Fabrication and Characterizations. The GO|PMMA multistack was fabricated by a spin-coating technique as shown in Figure 1a. GO, being the oxidized analogue of graphene, exhibits noteworthy properties on account of sp^2- and sp^3-hybridized carbon skeletons with a large number of functional groups including hydroxyl (−OH) and epoxy (−O) on either side of the sheet and carboxyl (−COOH) and carbonyl (−C═O) on the sheet edges.[20] The PMMA thin film was subjected to corona treatment for generating oxygen functionalities dangling on top of it. This assists in chemical adherence of subsequently spin-coated GO onto the PMMA thin film.

An earlier report[28] demonstrates a 470 nm PMMA thin film obtained by spin-coating PMMA (0.25g/mL dissolved in $CHCl_3$). Figure 1b indicates a 445 (±3) nm PMMA thin film that was obtained after corona treatment using the technique as shown in Figure 1a. Experimental details are discussed in the Experimental Section. Subsequently, the fabricated 1DPC of the GO|PMMA multistack was spin-coated with a final nanolayer containing the radiating dipoles. This was affixed to the hemicylindrical prism as shown in Figure 1c and excited through RK configuration.[29,30] The schematic presents a zoomed in cross-sectional view of different layers for a clear depiction of the modes sustained within the multistack. For an ease of comparative analysis of the acquired results, poly(vinyl alcohol) (PVA) was used as the standard polymer matrix to disperse the emitter dipoles for all the experiments in this study.[34,35] The unpolarized incident beam constituting TM (p) and TE (s) components and GraSE and GraPE emissions at 0° and at a wider angles, respectively, have also been depicted.

Broadly two methodologies were adopted for satisfying the phase matching condition in order to excite the SPPs at the metal-dielectric interface: (a) with prism-coupling and (ii) without prism.[2] While the latter was performed using a grating-coupling technique,[2] the former was performed in three different optical configurations, (i) Otto configuration,[2] (ii)

https://doi.org/10.1021/acsami.1c01024
ACS Appl. Mater. Interfaces 2021, 13, 17046−17061

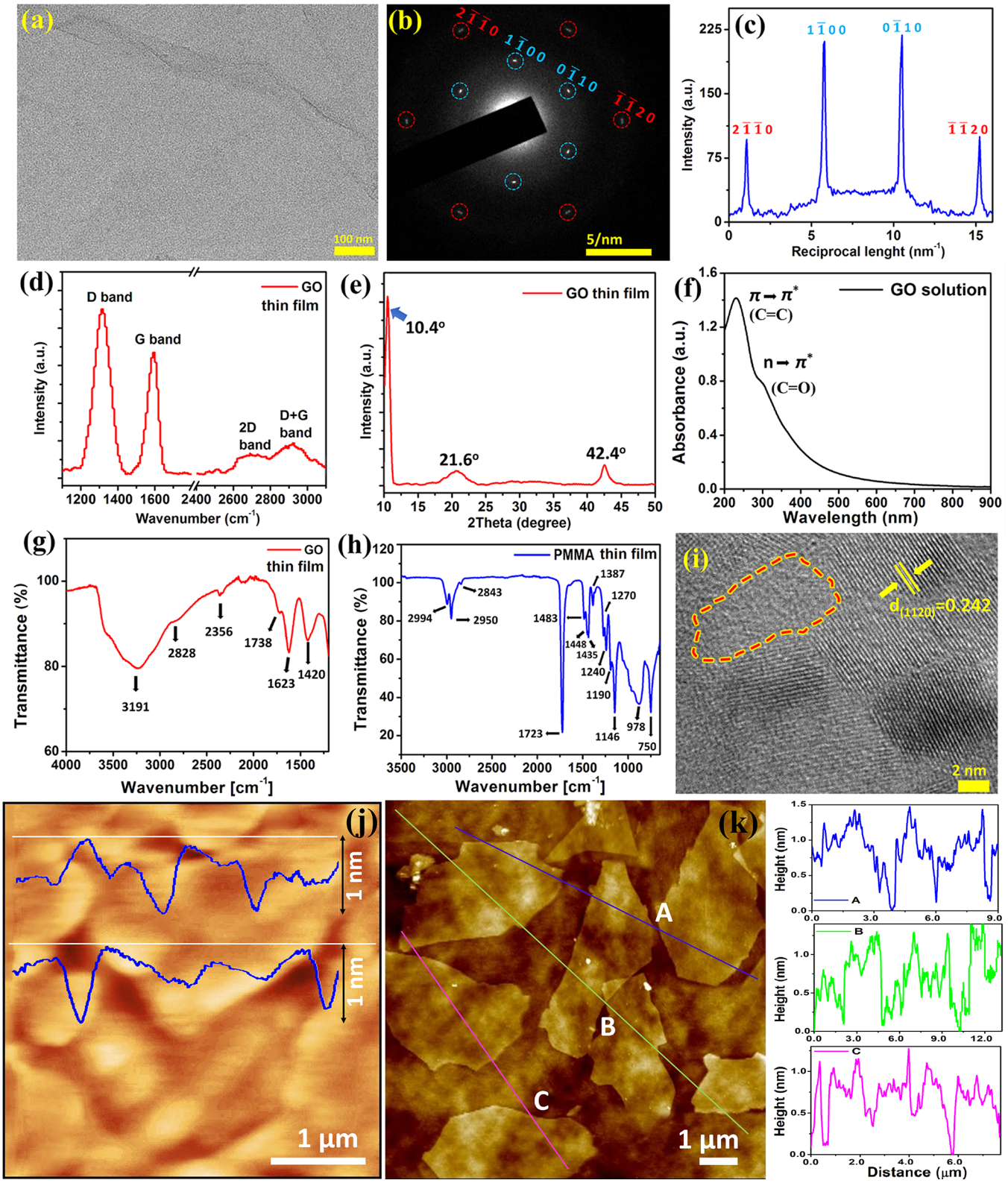

Figure 2. Optical and electronic characterizations. (a) TEM image of GO sheet. (b) SAED at the center region of (a) showing bright spots labeled with Miller–Bravais indices. (c) Intensity profile across the line-profile as presented in (b), including inner and outer diffraction dots. (d and e) Raman spectrum and X-ray powder diffraction (XRD) pattern of spin-coated GO. (f) UV–vis absorbance of GO dispersion. (g and h) Fourier transform infrared (FTIR) spectra of GO and PMMA. (i) HRTEM image of GO presenting regions of defects (curved dashed line). (j and k) AFM images of GO coating shown along with height profiles.

Kretschmann-Raether (KR),[2,23−25,36] and (iii) Reverse Kretschmann (RK) configuration,[36] and they are briefly explained below. In the Otto configuration, the prism and the metal thin film were separated by an air gap and was

https://doi.org/10.1021/acsami.1c01024
ACS Appl. Mater. Interfaces 2021, 13, 17046−17061

excited from the prism side. The thickness of the air gap was modulated to alter the coupling strength.[2] In the KR configuration,[2,23−25,36] the metal thin film was placed on top of the prism and in between prism and dielectric (or sample side). This was excited from the prism side, and the evanescent wave coupling with SPPs occurred at metal-dielectric interface by controlling the angle of incidence near the critical angle (for total internal reflection). That is, this requires the emplacement of a dielectric layer of high refractive index adjacent to the plasmonic substrate and an appropriate incident angle, θ_{SP}.[36] Furthermore, in the RK configuration (Figure 1c), the fluorescent layer (on metal thin film) was directly excited from the free space side.[23,36,51] This in turn excited the surface plasmons, and the emission was out-coupled at definite angles (from curved surface of prism) where phase matching was satisfied. We adopted RK configuration across all the experiments, in order to maintain generality across the results and for ease of experimentation and reliable comparative analysis, in line with our earlier works.[29,30,51] This requires the emplacement of a dielectric layer adjacent to the plasmonic substrate and an appropriate incident angle, θ_{SP}. Although π-plasmons supported by graphene apparently make it a semimetal,[18] obtaining the phase matching condition in the visible range remains a daunting task. In this context, we adopted a metal thin film-free, GO-based multistack architecture to access potential surface and bulk states of the multistack, as detailed in the subsequent sections. Figure 1d depicts a conceptual geometry adopted to increase the magnitude of k_x (x-axis wave vector component of the incident field) to equal or exceed k_{GP} (wave vector of the plasmon sustained by multistack), in turn realizing the condition for multistack plasmon resonance (MPR) [analogous to surface plasmon resonance (SPR)]. This was achieved by increasing the free space wave vector (k_o) [or decreasing the free space wavelength (λ_o) by λ_o/n_p, where n_p is refractive index of prism] with the incident light introduced from the prism side [KR configuration]. This implies that MPR occurs when $k_x = k_o\, n_p \sin\theta_{GP}$, where θ_{GP} (GP: graphene oxide plasmon) is the angle at which the multistack supports the graphene oxide plasmon polaritons.[36] It must be noted that, while graphene forms a continuous carbon framework of delocalized electrons, GO is present as flakes or islands.[20] However, for easy visualization we have used a continuous sheet to represent GO.

The examination of a dilute GO suspension that was drop-coated and well-dried on a lacey carbon supporting film with a transmission electron microscope (TEM) is shown in Figure 2a. The ultrahigh electron transparency of a very large surface area GO sheet with a few folds/overlaps with an adjacent GO sheet in the top part of the figure is evident. Figure 2b presents a 6-fold hexagonal array of diffraction bright spots seen with a selected area electron diffraction (SAED) study performed at the lower region of Figure 2a, displaying strong evidence for a graphene-like honeycomb structure for the sample under study.[37] Moreover, the relative intensity of the inner $1\bar{1}00$-type (blue) reflection being much more than that of the outer $2\bar{1}10$-type (red) reflection given with Miller−Bravais *hkil* notation in Figure 2c confirms the morphology of the sample to be a monolayer, consistent with earlier reports.[37,38] The d-spacings of the inner and out rings were found to be 0.21 and 0.12 Å, similar to the graphitic domains in graphene samples.[39] Moreover, one can note that the surface roughness (R_a) value of the PMMA film decreased after corona treatment, in consonance with an earlier report (Figure 1e,f).[39] The smoothened surface of PMMA thin film after corona treatment makes the surface more conducive for better bonding with a subsequently spin-coated GO layer.

Furthermore, Raman studies were performed to corroborate the nature of incomplete/partially oxidized GO flakes with the help of D-band (at 1338 cm^{-1}) and G-band (at 1596 cm^{-1}) intensities, as seen in Figure 2d. Several oxygen functionalities in GO cause a disruption of sp^2 bonds, attributing to structural defects (D-band) in the breathing modes of graphitic domains or whiskers like carbon (G-band). In line with earlier findings,[40] a relatively larger intensity of the D-mode (doubly degenerate phonon mode, E2g symmetry) compared to the G-mode indicates the presence of a GO monolayer in the spin-coated samples along with defects and vacancies. The regions of parent graphene domains present along with oxygen functionalities in the GO substructure (of graphene) was further validated from the X-ray diffraction (XRD) results shown in Figure 2e. Although crystalline graphite shows a d-spacing of 0.34 Å, the population of oxygen functionalities (epoxides and hydroxyls) and intercalation with water increases the interplanar separation to 8.49 Å with a sharp and distinct peak at $2\theta = 10.41°$, as seen in Figure 2e. While this accounts for regions of pure GO flakes, a broad and weak peak at $2\theta = 21.59°$ with a d-spacing of 4.11 Å indicates the presence of nonoxidized regions, as an incomplete oxidation of the graphitic framework.[41] Likewise, a weak peak at $2\theta = 42.45°$ [d-spacing: 2.12], even observed in the SAED pattern (inner bright spots) of the GO sample, substantiates that there are regions of graphitic delocalized sp^2 domains where the interconnection with oxygen atoms is absent completely.[41] The UV−vis absorbance spectra for the GO solution used for spin-coating are given in Figure 2f. This displays a maximum absorption at 229 nm and is due to $\pi-\pi^*$ transition of aromatic C═C bonds extensively present in GO flakes.[42] At slightly larger wavelengths (~300 nm), a shoulder was noticed. This is attributed to $n-\pi^*$ transitions of the carbonyl groups present in GO.[42] In addition to the above detailed HRTEM, SAED, Raman, and XRD studies, the Fourier transform infrared (FTIR) spectra for the spin-coated PMMA thin film and GO thin film show characteristic vibrational bands as given in Figure 2g,h. This provides an experimental verification of the fabrication protocol implemented and depicted in Figure 1c.

The presence of absorbed water molecules and alcohol groups (including phenolic OH) superimposed over the OH stretching frequencies of large number of carboxylic groups results in a broad absorption band in the region 3050−3800 cm^{-1}.[42] The large negative value of the ζ potential for the GO solution (−40.1 mV) indicates a stable dispersion with the presence of several negatively charged functional groups. This is on account of carboxylic acid groups in GO that also interact strongly with the corona-treated PMMA layer for maintaining the integrity of the multistack. While the vibrational bands at 2828 cm^{-1} account for asymmetric and symmetric CH_2 stretching, the band at 2356 cm^{-1} is due to CO_2 groups. A relatively strong absorption band at 1738 cm^{-1} is attributed to the stretching vibration modes of C═O in carboxylic acid and carbonyl groups. The assignment of stretching frequencies at 1623 and 1420 cm^{-1} was made to C—C skeletal vibrations of graphitic domains and C—O functionalities.[42,43] The vibrational stretching bands of PMMA are tabulated in Table S1 and discussed in detail in the Supporting Information (SI).

https://doi.org/10.1021/acsami.1c01024
ACS Appl. Mater. Interfaces 2021, 13, 17046−17061

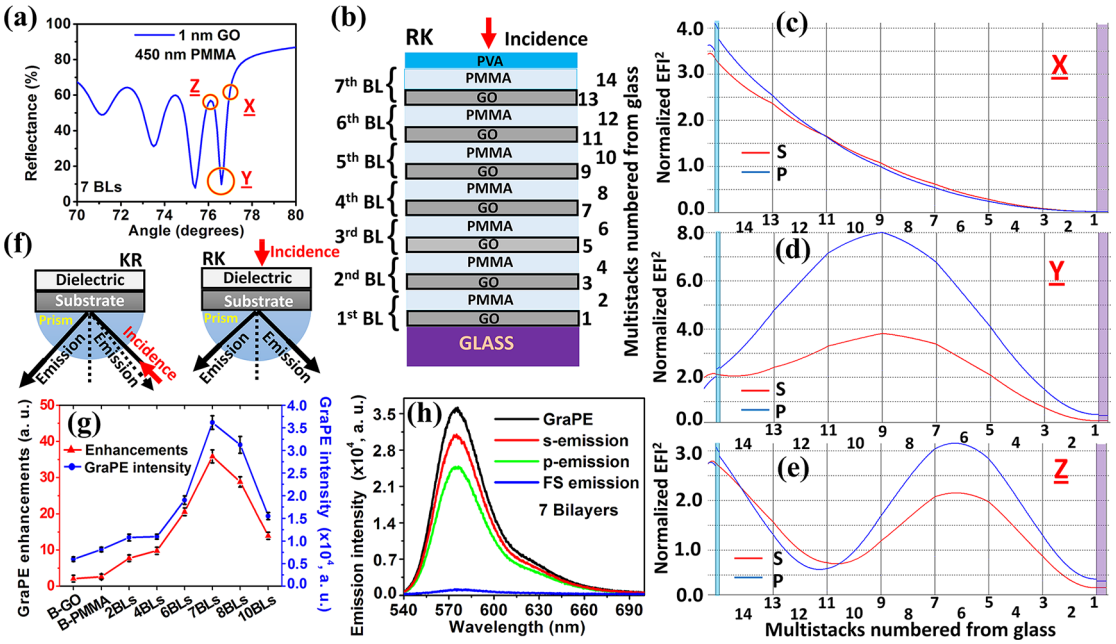

Figure 3. Graphene oxide plasmon-coupled emission (GraPE). (a) Reflectivity plot for the 7 BLs of the GO|PMMA multistack in the angle ranged from 70° to 80°, indicating two regions of high reflectivity [Z, X] and one region of low reflectivity [Y]. (b) Schematic of the fabricated multistack indicating the numbering of the same from glass toward PVA film, as adopted for EFI simulations. (c–e) EFI intensity profiles corresponding to the X, Y, and Z regions highlighted in (a). (f) Schematic of KR and RK configurations. (g) Correlation between GraPE emission enhancements [left *y*-axis] and emission intensity counts [right *y*-axis]. (h) GraPE emission intensity spectrum along with corresponding p, s, and FS emission spectra for the 7 BLs multistack architecture.

Yet another interesting and relevant feature of GO adopted for GraSP engineering studies is its intrinsic defects/vacancies/holes, as seen in Figure 2i. It can be clearly noted that the HRTEM image presents a highly crystalline region with a *d*-spacing of 0.242 Å, corresponding to the (1120) lattice fingerprints of graphene. The intensity of the D-band being more than that of the G-band strongly suggests the presence of defects in the graphitic domains. The peculiar characteristics of the defects were explored by Raman signal enhancement on account of enhanced local electric field intensity.[40,43] In this context, we observe structural defects in Figure 2i, marked with a curved dashed red line, having no lattice fringes of parent graphene. Earlier reports also suggest the presence of holes in GO on account of CO_2 and CO functionalities present along with carbonyl groups accounting for boundaries of such holes.[44] Therefore, we confirm that the GO sample used in the current study has large regions of unstrained sp^2 bonds, preserving the order and hexagonal symmetry of original graphene sheet with fewer regions of oxidized counterparts having nominal sp^2 bonding features along with defects.[37−41,44] We have deliberately chosen this composition of GO (neither pure graphene nor pristine GO) that presents both oxygen functionalities and large graphitic areas in order to achieve an appreciable amount of π plasmon−π plasmon hybridization within a single layer of GO thin film. Furthermore, we extensively studied the surface morphology of monolayer GO using AFM characterization (Figure 2j,k), with details presented in the SI (Figure S1).

Graphene Oxide Plasmon-Coupled Emission (GraPE) Analysis. Inspired by research undertaken by Lakowicz et al.,[23−25,36] SPCE has gained strong foothold in the broad arena of plasmonics with important studies, processes and applications at nanodimensions.[29,30,34] Recent research advancements[45] in SPCE domain continue to utilize metal-based plasmonic substrates for chem-bio sensing frameworks: single molecule detection,[46] bimetal mediated-DNA diagnostics,[47] femtomolar glutathione[29] and spermidine sensors,[30] label-free aptasensors,[48] to name a few. However, owing to the lossy nature of metallic substrates that directly affect the performance of plasmonic sensors, alternative plasmonic substrates[3,6,28] have gained increased attention, photonic crystal being one of them.

Eli Yablonovitch and Sajeev John in the year 1987 introduced the term photonic crystal,[21] which was followed by extensive scientific reports portraying unique advancements in the field of multidimensional PCs.[7,21,23,24] In brief, distinctive properties rendered by stopbands, BSWs, IOM, band edge, and leaky modes have revolutionized the means to exploit and employ EM-field in the broad arena of nanophotonics. Photonic crystals have recently found widespread applications in structural color printing, fiber optics, sensing, optical devices, and photovoltaics, to name a few.[5,49] After the advent of PCs, in a span of 10 years, Boehm et al. referred to planar hexagonal carbon lattice as graphene,[50] following which there has been tremendous attention in its translational research[4,7] on account of its unique strength, carrier mobility, and chemical, optical, and thermal properties.[14,18,28] From an extensive survey of the literature, it can be concluded that, although several applications of graphene and graphene oxide have been reported in the broad area of optics and photonics, to the best of our knowledge, their ability to replace metal thin films by generating surface EM waves has not been discussed, after their preliminary observation in the year 2012.[28] Unlike the graphene framework utilized earlier, here, we developed an economically viable and user-friendly GO-based multistack to not only observe directional emission but also achieve expedient steering[25] emission in the complete absence of

https://doi.org/10.1021/acsami.1c01024
ACS Appl. Mater. Interfaces 2021, 13, 17046−17061

metal thin films. Further, the purpose and motivation for carrying out this work is elaborately discussed in the SI.

Regions/angles of sharp resonance dips in the reflectance profile are well-established to denote the coupling of luminophore emission (fluorescence, phosphorescence, chemiluminescence, or photoluminescence) with the incident radiation in SPR studies.[34,35,45−48] As seen in Figure 3a, for 7 bilayers (BLs) of GO and PMMA, a directional emission can be expected due to a strong SPR dip at a wider angle (76.6°). This is attributed to phase matching achieved with the use of the GO|PMMA multistack that in succession assists the coupling of radiating dipoles with the truncated multistack.[36] Furthermore, the effect of the number of BLs of GO|PMMA on the intensity of resonance dips obtained using TFCalc simulations is presented in Figure S2. It is seen that, although the dip in the reflectivity does not vary significantly at 0°, the percentage reflectivity decreases at higher angles as the number of BLs increases. For clarity in presentation, the reflectivity profiles for 1, 2, 3, 4, 5 BLs and 6, 7, 8, 9, 10 BLs were plotted separately in Figure S2a,b. A lower number of BLs yield smaller resonant dips and sharpness of the dip increases for higher BLs. Although 6, 7, 8 BLs show similar minimum reflectance, the multistack with 7 BLs shows a double dip with nearly equal intensities, absent in lower BLs. Hence, on the basis of simulations, we expect to observe a maximum emission intensity from radiating dipoles on a substrate having 7 BLs in comparison with the rest, as increased thickness in higher BLs is expected to contribute significantly to back scattering and reduced enhancements.[56,57] Additionally, the possibility of the FS emission to increase is more for a larger number of BLs, which may also contribute for reduced emission enhancements for larger thicknesses or a larger number of BLs. For all the simulation studies, the real and imaginary parts of the refractive index of GO and PMMA were taken into consideration and provided as input parameters for generating electric field intensity (EFI) and reflectivity plots.

BGCE studies have shown increased density of states (DOS) for emitter dipoles placed in its vicinity. In this context, we adopted standard TFCalc simulations[23,24] to understand the EFI at each of the multiple resonances (and corresponding crests) observed in Figure 3a, labeled as X, Y, and Z. A schematic representation of the engineered 7 BLs multistack is shown along with the numbering from the glass slide to the PVA layer in Figure 3b. The layers numbered with odd and even numbers correspond to GO and PMMA layers, respectively. This also holds good for the numbering in the EFI profiles throughout. The modes that have not been carefully investigated previously[28] present interesting states that are hybridized, making them ideal candidates for light energy confinement. The EFI plots are captured in Figure 3c−e. The larger angle crest (Figure 3a) with a high reflectivity indicated as X in Figure 3c presents a strong surface state. This is due to the nonlinear nature of the multistack architecture sustaining solitons[14−17] that are analogous to Tamm states[24−27] observed in conventional PCs. This is because Tamm states are observed for conventional photonic crystals made of dielectrics where the EFI resembles the one that is seen in Figure 3c. Further, a sharp resonance dip at Y of Figure 3a is shown to support a bulk mode within this multistack with a maximum EFI confined relatively in the center of the multistack (Figure 3d). This is in good resemblance with the EFI profile reported for standard MDM[35] cavity modes, where the dielectric sandwiched between the two metal thin films presents a similar EFI response. This clearly indicates that the angle of minimum reflectance in the GraPE substrate is on account of multistack sustaining bulk modes analogous to those of the MDM modes. The pseudometallic nature (discontinuous, delocalized π-plasmons of GO sheets with defects) inherited from π-plasmons[37−40] of individual GO sheet could be responsible for such a phenomenon. This is further on account of plasmon hybridization between aggregation resistant GO flakes in a single sheet.[13−16,20] The evident observation of an increase in emission enhancements obtained with an increasing number of BLs in the multistack specifies that plasmons of one BL interacts with those of an adjacent BL. This understanding is in line with the ability of the graphene-based multistacks or multilayers to support solitons (nonlinear attributes to that of Tamm states), as reported earlier.[14−18] This can be further understood by observing the characteristic behavior of multiple dips obtained in the reflectivity plots (Figure S2). For one BL, we observe one dip, for two BLs, two resonance dips, and so on. The concept of hybridization between two graphene sheets separated by a dielectric resulting in symmetric and antisymmetric hybridized states has been reported earlier.[12−15] In this context, we propose an extended hybridization between plasmons supported by individual BLs across the multistack (in between the BLs).[12−14,33] Additionally, with a reduction in angle (at Z), a bulk mode as well as a surface mode were observed. This indicates that, as the angle moves away from the region of maximum resonance (maximum dip), bulk and surface modes begin to hybridize.[12,13] In other words, solitons (on account of nonlinearity) and hybridized plasmons (due to linear property) interact with one another to present multiple resonant dips and crests in the reflectivity profile. This trend in EFI is constantly observed with resonant dips and crests at lower angles (less than 70°, but greater than 50°) and is presented in Figure S3. Hence, we conclude that, although earlier reports have demonstrated BGCE enhancements distinctly at lower and higher angles due to BSWs and IOMs, respectively,[23,24] the GO|PMMA multistack, due to a synergistic combination of plasmons (from pseudometal) and nonlinear solitons, presents a hybridization of bulk and surface states resulting in multiple resonances. The importance and details of reflectance at different wavelengths are given in Figures S4−S6.

It is customary to obtain highly polarized and >50% signal collection of directional luminescence in SPCE platform due to in-phase coupling between TM-polarized excitation field and surface plasmon oscillations on a metal-dielectric interface.[29,30,36,45−48] The SPPs generated as an immediate outcome of this coupling have an evanescent behavior. An emitter dipole placed in its vicinity experiences EM-field confined to the surface, resulting in 5−10-fold enhanced emission of emitter dipoles in SPCE.[29,30,36] As predicted theoretically, with the use of multistacks (instead of a metal thin film) in a conventional SPCE framework, we observed an increase in the emission intensity with an increasing number of BLs spin-coated on top of a glass substrate. Particularly with the use of 7 BLs of GO|PMMA, an increase up to 35-fold in emission enhancements was observed (Figure 3g). In line with earlier reports,[29,30,36] the emission enhancements were calculated as a ratio of GraSP [i.e., in the case of both GraSE and GraPE] emission intensity counts to free space (FS) counts. It is worth mentioning that this is the first time such augmented enhancements have been experimentally

https://doi.org/10.1021/acsami.1c01024
ACS Appl. Mater. Interfaces 2021, 13, 17046−17061

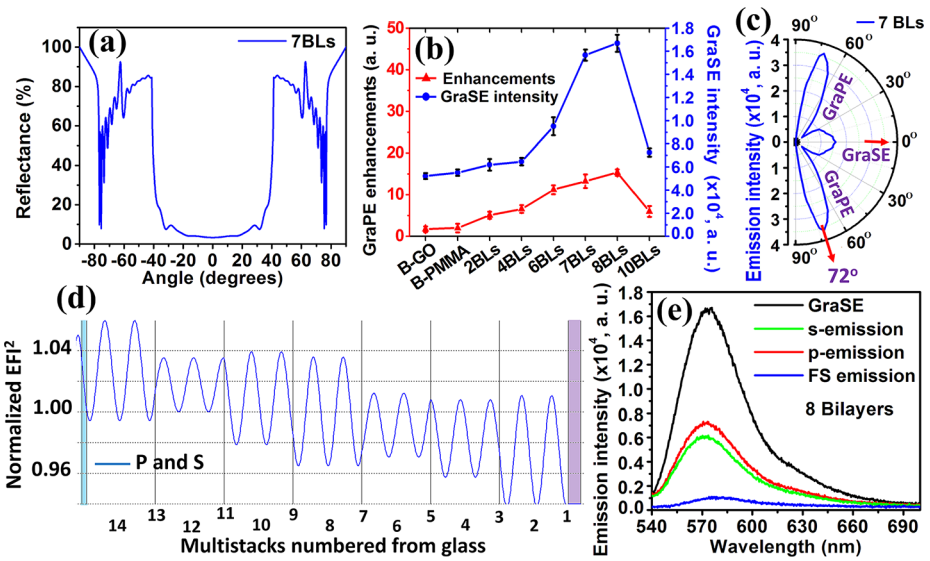

Figure 4. Graphene oxide plasmon-coupled soliton emission (GraSE). (a) Reflectivity plot for 7 BLs of GO|PMMA multistack in an angle range from −90° to +90°, indicating two regions of high reflectivity at wider angles with multiple narrow dips and a broad angular region of high reflectivity around 0° (b) Correlation between GraSE emission enhancements [left *y*-axis] and emission intensity counts [right *y*-axis]. (c) Experimentally obtained angular emission pattern at distal part of the prism with beaming emission at 0° and directional emission at 72° in correspondence with the reflectivity shown in (a). (d) EFI profile at 0° showing an increase toward the surface of the substrate. (e) GraPE emission intensity spectrum along with the corresponding p- and s-polarized emission and FS spectra for 8 BLs of the multistack architecture.

demonstrated on a metal-free platform through a simple spin-coating substrate fabrication. This amplification is substantial on account of the following factors: (i) lossless nature of GraSP engineering in comparison with conventional SPCE, as the self-induced lossy nature of metals results in damping of theoretically postulated extreme and tight optical energy trapping. (ii) The synergistic effect of nonlinear solitons and linear π-plasmons[14,20] account for surface and bulk states. (iii) In the case of metal-dependent SPCE studies, only emitter dipoles oriented perpendicular to the metal surface couple with surface plasmons to give TM-polarized emission.[29,36] However, in case of the GraSP platform, radiating dipoles oriented not only perpendicular to the surface but also nearly parallel to the multistack couple with surface and bulk states supported by this architecture, thereby resulting in enhanced TE- and TM-polarized emissions. This phenomenon of graphitic frameworks that aid the coupling of radiating dipoles oriented in every direction, other than perfectly parallel to the metal thin film, has been reported earlier.[51] The GraPE intensity spectra for all BLs (2−10) along with their p- and s-polarized emission and FS spectra are presented in Figure S7.

While traditional SPCE supports only p-polarized emission, HRI dielectric NPs placed atop a metal thin film sustain strong magnetic flux dipoles, resulting in a highly s-polarized emission.[3] Similarly, PCs display the coupling of s-modes due to alternating HRI and LRI nano thin films.[23] However, a multistack architecture for coupling both p- and s-polarized modes is unfamiliar. In this context, GraPE engineering presents a unique architecture for the coupling of unpolarized light where the TE-mode is marginally superior to that of TM-coupling, as seen in Figure 3h. The TM- and TE-polarized EFI profiles presented in Figure 3c−e confirm this understanding. Although both p- and s-polarized modes are continuous within the stack, at the surface near the terminating PVA layer (embedded with radiating dipoles), the p-modes are predominantly noncontinuous and fragmented. This implies that the extent of realizing p-mode coupling is diminished.[23,24]

Graphene Oxide Plasmon-Coupled Soliton Emission (GraSE) Analysis. The reflectivity plot obtained for a complete angular range, from −90° to 0° to +90°, is shown in Figure 4a. Resonance dips at a higher angle have been elaborately discussed in the preceding section on GraPE engineering. Here, we attempt to understand the property of resonance dip, in reflectivity at 0°. In a traditional SPCE platform, the emission observed at 0° is termed as beaming/steering emission. This comes with an important advantage of no requirement of a rotational stage, generally employed for the collection of directional emission in the SPCE platform.[25] In the case of beaming emission achieved with MDM frameworks, the detector was fixed in line with the incident light beam. Since fluorescence emission travels in same straight line as that of the incident ray in RK configuration, the SPCE platform layout is immensely simplified. Further, the usage of 1DPCs on a metal thin film also presents beaming emission on account of Tamm states.[25,26]

In this study, we used GraSE engineering for the steering of emission with augmented emission enhancements for 8 BLs multistack (Figure 4b). In consonance with the simulated reflectivity plot (Figure 4a), the experimentally obtained angularity plot in Figure 4c shows characteristic directional (72°) as well as beaming emission (0°). We see a 5°−7° variation from the simulated value for GraPE. This is primarily on account of the approximation made during simulation, where GO was considered as a continuous film with a thickness of 1 nm. However, unlike pristine graphene, GO presents a noncontinuous thin film due to its well-established intrinsic properties discussed in previous sections. Further, infinitesimal imperfections in the fabricated multistack could also lead to such a mismatch. The angularity plot representing the emission intensity counts collected at distal part of the prism with a 2° resolution is presented in Figure 4c. We observed a clear beaming emission at 0° and directional emission at 72°. In Figure 4a, we observed a significant dip in reflectivity even at 0°, as observed with MDM[25] and Tamm

https://doi.org/10.1021/acsami.1c01024
ACS Appl. Mater. Interfaces 2021, 13, 17046−17061

state-coupled emission (TSCE) frameworks.[24] The EFI profile presented in Figure 4d confirms its origin and functionality as a surface state, resembling the TSCE phenomenon in conventional dielectric-based photonic crystals. This indicates that the surface state generated at the PVA layer doped with radiating dipoles experiences high EM-field enhancements even at 0° on account of solitons.

Moreover, it must be noted that RK configuration is an essential requirement to observe beaming emission[27,35] at 0°. This is in good agreement with the simulated reflectivity plot (Figure 4a) having the dip in reflectance at 0°. For better clarity, the EFI profile at 0° for only the PMMA stack (without GO) and the GO stack (without PMMA) is presented in Figure S10 for 7 BLs. This establishes that, without the multistack architecture with alternating HRI (GO) and LRI (PMMA) materials, EFI remains constant from the glass slide to the outermost PVA nanolayer. To the contrary, we observed in Figure 4d that EFI shows a gradual increase from the glass slide to PVA through the multistack. This is in close agreement with the previously reported surface EM waves supported by the multistack with graphene as HRI.[28] Although 15-fold emission enhancement obtained with 8 BLs is maximum, it is slightly more than that obtained from the 7 BLs multistack. Nevertheless, this increase up to 15-fold is a significant result when compared to that achieved with conventional SPCE. Subsequently, for maintaining generality in the study, we have carried forward the GraSP emission engineering with a variety of NPs using the 7 BLs multistack alone. The fluorescence emission spectra displaying high intensity counts in comparison with FS emission along with the p- and s-polarized emission are presented in Figure 4e. The GraSE intensity spectra for all BLs (2−10) along with their p- and s-polarized emission and FS spectra are presented in Figure S11.

Another interesting feature of GraSE engineering is the polarization of modes presented by multistack at 0°. In Figure 4d, both p- and s-modes are presented with a blue line, since they both have exactly similar behaviors inside and at the surface of the multistack. With this background, one can clearly speculate an equally enhanced emission of both p- and s-polarizations. In strong agreement with this, we observed nearly equal p- and s-polarized emission enhancements at 0°, as seen in Figure 4c. The angularity plots for all BLs displaying both beaming emission and directional emission are presented in Figure S12. We conclude here that the increase in emission enhancements compared to FS emission is on account of the hybridized modes (π-plasmons and solitons) sustained by the multistack for GraPE. While for GraSE, the enhanced emission is on account of solitons. Furthermore, we also performed MATLAB-based numerical simulations in line with our earlier works[34] to obtain the dispersion diagram for the proposed multistack architecture for 7 BLs (Figure S13). The results from the dispersion diagram are in consonance with the results obtained from the TFCalc simulations, where we observed multiple resonances at higher angles and also dip in reflectivity at 0°. In addition to this, the distinctive properties of this platform with futuristic scope are detailed in the SI (Figures S14−S18).

Metal, Intermetallic, Rare-Earth, and Carbon−Metal Hybrid NPs for Cavity Hot-Spot Generation. The 35-fold emission enhancements realized with 7 BLs multistack architecture were further augmented using cavity engineering at the multistack interface to understand the effect of different types of plasmonic and dielectric NPs toward hot-spot generation. The large tunability in emission enhancements has been demonstrated using a wide variety of NPs: metals, Ag, Au, and Pt; intermetallics, SiO_2, TiO_2, TiC, TiN, and TiCN; rare-earth, Nd_2O_3; low-dimensional carbon substrate−plasmonic hybrids, CDs. AgCDs were interfaced with the fabricated multistack such that the radiating dipole is sandwiched in the cavity environment. This study opens a new horizon for understanding plasmonic coupling and provides a futuristic innovation of hybridized metal-dielectric platforms. The variable EM-field entrapment provided by these NPs and the extended hybridization between the hybridized modes of multistack and resonances sustained by individual NPs result in tailored PFs with a wide range from 4.4 to 471.6 for SiO_2NPs and AgCD NPs, respectively, in the GraSP emission platform. The direct effect that the cavity environment has on the spontaneous emission from a radiating dipole is known as the Purcell factor.[29] Cavity hot-spots with amplified EM-field intensity result in a decrease in fluorescence lifetime, an increase in radiative decay rate, an enhanced quantum yield, and a high PF.

Purcell-enhanced excitonic emission from cavity-modified photonic nanoregimes has presented impactful and fascinating aspects of light−matter interactions in van der Waals heterobilayers.[52] The materials display unique and judicious properties in bulk as well as nanoscale dimensions.[53,54] We have earlier demonstrated the utility of a variety of nanoparticles (NPs) and nanocomposites in a SPCE platform to comprehend their unique plasmonic properties. Physicochemical interfacial interactions were harnessed in nanocavities (between NP and metal thin film) to realize the femtomolar sensitivity of glutathione[29] and spermidine[30] and the picomolar sensitivity of a coronary $LpPLA_2$[51] biomarker. In this context, a cavity environment sustaining EM hot-spots, generated between the NPs and metal thin film, was exploited for different useful applications.[29,30,51] As a continuation, in this work, we intended to understand the intricate details of interfacial plasmonics using different types of NPs on a metal-free GraSP platform, unlike the conventional SPCE platform, presenting intriguing results.

HRTEM images of all the NPs used for the GraSP (GraPE and GraSE) engineering studies are presented in Figure 5. The lattice resolved images indicating the characteristic d-spacing are also shown. The TEM images of all NPs at different resolutions along with SAED images and corresponding powder XRD patterns are presented in Figures S19−S22. The discussions pertaining to Miller indices, 2θ positions, ICSD reference code, and the crystal system have also been given in detail (Supporting Information). From Figure 5l, we see that AgCDs presented a maximum of 947-fold and 573-fold enhancements with GraPE and GraSE. Colossal use of AgNPs for plasmonic investigations involving newer frameworks such as metal-dielectric hybridized plasmons, void plasmons, and truncated plasmons is now on the rise.[1−3] In this context, we synthesized AgCDs as described in an earlier report.[51] These nanohybrids present multifold hot-spots due to two important aspects: (i) Ag being a metal and CDs being a dielectric; the metal−dielectric hybrid of AgCD presents hybridized plasmonic resonances.[51] From Figure 5m, we see that synthesized CDs and AgCDs gave absorbances at 271 and 458 nm. Also, the HRTEM image in Figure 5k shows an overlapping d-spacing of AgNPs and CDs, confirming the formation of hybrids. To the best of our knowledge, this is the first report that presents >900 emission enhancements on a

https://doi.org/10.1021/acsami.1c01024
ACS Appl. Mater. Interfaces 2021, 13, 17046−17061

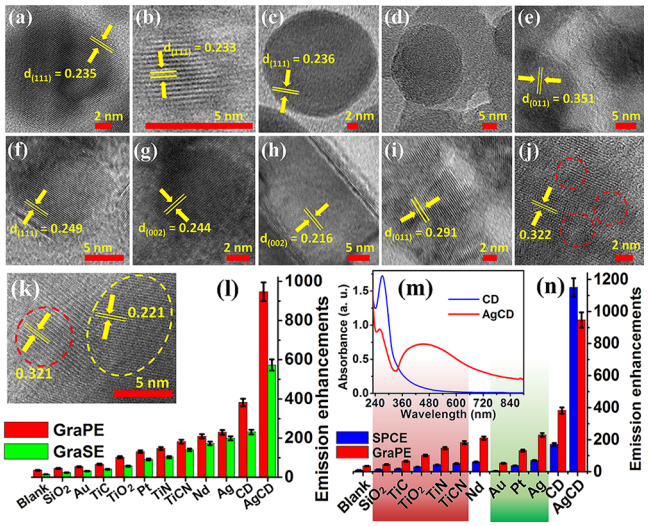

Figure 5. Tunable emission enhancements with different nanomaterials. HRTEM images of (a), Au, (b), Pt, (c) Ag, (d) SiO_2, (e) TiO_2, (f) TiC, (g) TiN, (h) TiCN, (i) Nd_2O_3, (j) CDs, and (k) AgCDs nanoparticles. The *d*-spacing has also been presented for crystalline NPs. In (k), the red dashed curve and yellow dashed curve represent CDs and AgNPs. (l) Comparison between GraPE and GraSE enhancements for all the NPs. (m) UV−vis absorption spectra for CDs and AgCD. (n) Comparison between GraPE and SPCE enhancements for the dielectric (red shaded), rare-earth (unshaded), and metal (green shaded) NPs used.

metal-free substrate. The absorbance of CDs in AgCDs lessened on account of the utilization of CDs for AgCD formation. During the process, the CDs are decorated with AgNPs, hence red-shifting the absorbance maximum of AgCD hybrids to 458 nm. (ii) As a result of the decoration of CDs, the EM hot-spots generated are multifold. This is because the nanogaps between the AgNPs and the CDs support intense EM-field confinement. The voids and nanojunctions that are generated as an offshoot of this decoration between the decorated AgNPs would further enhance the optical field entrapment. Adding to these hot-spots, when AgCDs are taken in vicinity of GraSP substrate, they experience and work in tandem with the surface and bulk states presented by the multistack. Likewise, the radiating dipoles sandwiched between the multistack and AgCDs experience large EM-field intensity on account of multiple hot-spots from NPs and surface and bulk states from the multistack. Theoretically, this results in a very large PF of 471.6 for AgCDs in the GraSP emission platform. In strong agreement with the theoretical data, we observed amplified emission enhancements. Also, we observed that emission enhancements obtained from directional GraPE were always more than those of beaming GraSE. This is reasonable since the EFI profile, as discussed earlier, was, in general, lesser for GraSE in comparison with that of the GraPE framework. Besides, the emission enhancements seen in Figure 5l are in excellent agreement with the PF obtained by taking these NPs on the GraSP substrate.

Figure 5n shows the comparative analysis between the performance capabilities of SPCE and GraPE technologies. It is clearly seen that, with the use of any NP (other than AgCDs), the emission enhancements obtained were superior in the case of GraPE as compared to GraSE. This augmentation in enhancement is because of the lossless nature of GraPE architecture compared to that of lossy metal-dependent SPCE. In fact, the hybridized states of solitons and π-plasmons presenting bulk and surface states that are absent in the case of metal thin film would aid the coupling phenomenon here to a significant extent. However, it is to be noted that emission enhancements seen with GraPE engineering remained marginally less compared to the SPCE enhancements obtained with the use of AgCDs. Although the exact mechanism for this observation is still under inspection, one plausible explanation could be that radiating dipoles held in the infinitesimal volume between CD, AgNP, and Ag thin film could experience amplified EM hot-spots due to an extended hybridization of metal thin film metal AgNPs−dielectric CDs−metal AgNPs, wherein the continuity in the dielectric constant is not significantly broken. This could lead to an extremely cooperative and coherent interaction between the LSPR of AgNPs, dielectric plasmons of CDs, hybridized plasmons of AgCD, void plasmons between AgNPs, and most importantly the propagating plasmons of Ag thin film, thereby boosting and outdoing the capacities of GraPE. Whereas, in the case of GraPE engineering when AgCDs are taken on its surface, the mismatch in the dielectric constant is comparatively much larger because of the dielectric multistack-metal AgNPs−dielectric CDs−metal AgNPs framework. These observations were validated by the PFs obtained with the use of AgCDs in SPCE (1027.6) and GraSP (471.6) emission platforms, where we clearly noticed that the PF in the cavity hot-spot was larger for SPCE. Theoretical studies and experiments to comprehend the contribution from each of these EM-field augmenting parameters are underway. While the dielectrics and intermetallics have shown to assist in large tunable PFs on the SPCE platform [SiO_2, 35.9; TiCN, 109.52; CD, 114.12; Au, 3464.7], we noticed that the PFs on the GraSP platform [SiO_2, 4.39; TiCN, 3.99; CD, 19.45; Au, 5069] are moderately enhanced, resulting in reasonably higher emission enhancements. It is well-known that AuNPs result in quenching of emitter dipoles placed in their vicinity.[30,35] In similar lines, we observed the quenching of emission from RhB, resulting in 5-fold emission enhancements in SPCE. This phenomenon has been exploited in biosensor applications for the sensing of aptamers on a quenching−dequenching SPCE platform.[48] In contrast to this, we observed an enhanced emission of 53-fold (compared to a blank of 35-fold) while AuNPs were taken in a cavity architecture in GraPE. This is noteworthy since the lossless nature of metal-free multistack aids in the coupling of dipoles that are otherwise quenched. This unique observation can be rationalized by taking into account the competitive effect of the bulk and volume EM-field confinement modes sustained by the multistack and dequenching effect. The increase in theoretically obtained PF (5069 in GraSP vis-à-vis 3464.7 in SPCE) and experimentally obtained emission enhancements confirms that the quenching factor is outdone by hybridized modes and coupling interactions with LSPR of AuNPs, thereby presenting a quench-free Au-cavity framework. This is, indeed, a crucial strategy to overcome the quenching effect of AuNPs and has tremendous scope for next-gen plasmonic applications. Optical light scattering effects from Nd_2O_3 nanorods (NRs), acting as "Huygen" sources for enhanced forward scattering outdoing the metallic AgNPs on a SPCE platform have recently been studied for evaluating hazardous tannic acid in environmental water bodies.[55,56] The results of the current study being preferable and superior in comparison with SPCE for sensing applications, again, present a new outlook to understand the effect of several other

https://doi.org/10.1021/acsami.1c01024
ACS Appl. Mater. Interfaces 2021, 13, 17046−17061

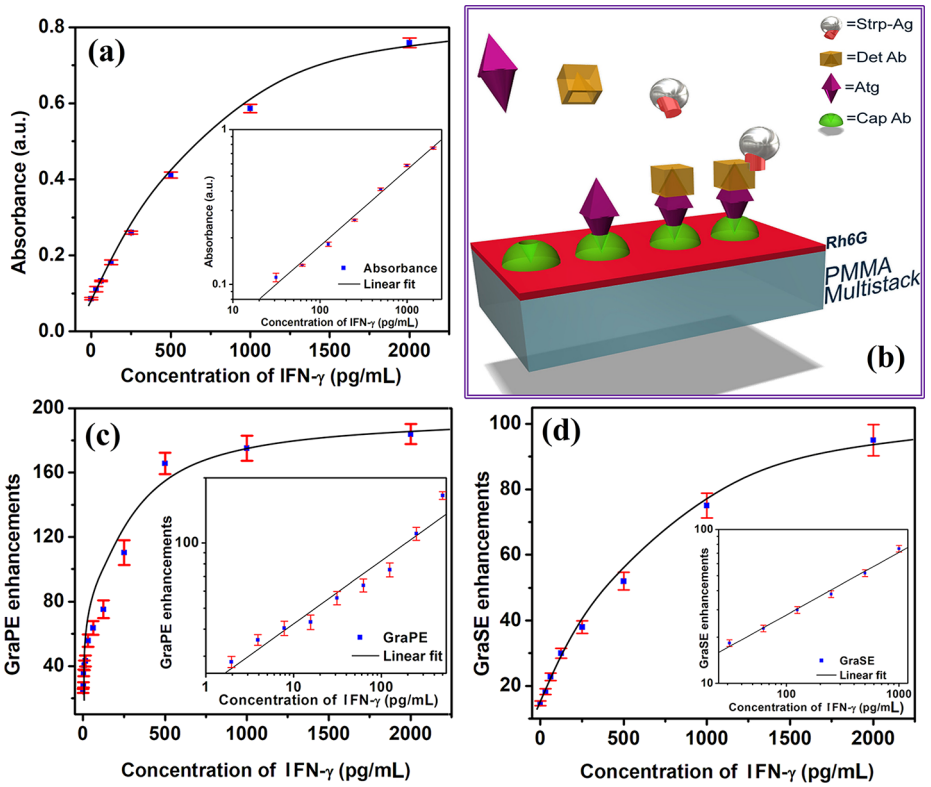

Figure 6. Biosensing with GraSP emission platform. Calibration curves of antigen (human interferon-γ, IFN-γ) concentration versus (a) absorbance values obtained in a conventional 96-well plate ELISA. (b) Conceptual schematic of ELISA performed on the multistack, (c) GraPE enhancements, and (d) GraSE enhancements. The insets shown in each of the plots indicates a linear relationship on a bilogarithmic coordinates.

lanthanides and actinides on the GraSP substrate. Further, Al^{3+} ion and cortisol sensing that have been achieved using the nanocavity supported by the Bloch surface waves of 1DPC and the LSPR of plasmonic NPs can also be explored in the GraSP platform because of the advantage of simple substrate fabrication involved here.[55,56] Additionally, this platform can be used for sensing applications and monitoring hazardous elements in food, body fluids, and environmental water bodies.

On a concluding note, we attempted to compare and contrast the emission enhancements obtained by using metallic, intermetallic, rare-earth, and low-dimensional carbon and composite substrates. This report provides a broad overview of GraSP engineering using NPs that are from different elements of the periodic table. Despite this, several other NPs that involve magnetic NPs, ferroelectric NPs, nanovesicles, alkali and alkali-earth NPs, polymeric NPs, and their hybrids need to be studied on the GraSP substrate to understand the impact and novelty brought by this unique architecture. The obtained results showcase a new trajectory for beneficial and practical output for sensing applications in the growing field of plasmon-coupled emission spectroscopy.

Biosensing Applications of GraSP Emission Platform. Further, we demonstrate the importance of the interfacial GraSP emission platform (in comparison to conventional ELISA and SPCE) in monitoring the human interferon γ (IFN-γ) antigen concentrations through a sandwich immunoassay. The human IFN-γ is one of the different types of endogenous proinflammatory cytokines and plays a crucial role in human health and illnesses.[57] Host protection is primarily dependent on an innate and adaptive immune system. While natural killer (NK) cells and natural killer T (NKT) cells are major producers of IFN-γ via innate immune response, $CD4^+$ T cells and $CD8^+$ T cells contribute to IFN-γ production during an adaptive response.[57,58] The vital functions of this type II interferon includes antiproliferative and antiviral effects, immunostimulatory and immunoregulatory properties, and antiparasitic effects during disease progression.[57−60] Elevated levels of IFN-γ in the human body is characteristic of several diseases such as cancer, Crohn's and Johne's disease, tuberculosis, Diabetes mellitus, HIV, dengue, and chronic obstructive pulmonary disease (COPD) to name a few.[61−63] Therefore, IFN-γ has been widely adopted as a biomarker for early diagnostics and medical treatment. The majority of these disease states demand picomolar sensitivity of IFN-γ in order to confirm the cause for specific illness in patients. Sandwich enzyme-linked immunosorbent assay (ELISA), reverse transcriptase polymerase chain reaction (RT-PCR), and enzyme-linked immunospot assay (ELISPOT) are the widely used methodologies for the detection of human IFN-γ at biologically relevant concentrations.[60−63] ELISA is well-known for its innate reliability, sensitivity, specificity, and reproducibility of results. Moreover, the SPCE platform has been earlier utilized for performing such sandwich immunoassays, extending their utility in biosensing applications.[48,64,65] In light of these observations, in this report, we attempt to establish the GraSP emission platform as an efficient alternative for SPCE and conventional absorbance-based ELISA applications. The experimental details of ELISA performed via absorbance, SPCE, and GraSP emission platforms are presented in the Experimental Section. In brief, SPCE and GraSP emission platforms were spin-coated with a 5 nm PMMA polymer thin film layer doped with Rh6G radiating dipoles. The capture (coating) antibody was immobilized on to this, and a sandwich ELISA was built using IFN-γ, a biotinylated detection

https://doi.org/10.1021/acsami.1c01024
ACS Appl. Mater. Interfaces 2021, 13, 17046−17061

antibody. Furthermore, streptavidin conjugated AgNP was added for the generation of hot-spots. Higher concentrations of antigen assisted in the formation of a large number of hot-spots between the AgNP and metal thin film (in case of SPCE) as well as the PMMA|GO multistack (in the case of GraSP). As discussed in preceding sections, the nanogaps between the metal thin film or the GraSP platform and the metal NP are the regions of high electric field intensity and are called hot-spots.

Figure 6 shows the calibration curves obtained for the detection of IFN-γ using different detection methodologies. The conventional absorbance-based 96-well plate ELISA yielded a linear relationship between the absorbance and different IFN-γ concentrations. This is presented as an inset in Figure 6a, where we observed a linear fit on a bilogarithmic coordinates[48] with an R value of 0.988 and a linear range from 31.25 to 1000 pg mL^{-1}. The limit of detection that could be achieved here is 20.4 pg L^{-1}. On account of high sensitivity of the SPCE platform, as expected, from Figure S23 (and the inset provided), we noticed a linear relationship between the SPCE emission enhancements obtained and different concentrations of IFN-γ.[48,65] Here, we observed a linear fit in the range 7.81−250 pg mL^{-1} (R = 0.987), and the limit of detection was further lowered to 7.81 pg mL^{-1}. Furthermore, it is worth noting that the maximum emission enhancement observed with 2000 pg mL^{-1} (maximum concentration of antigen) in SPCE is 112-fold. The conceptual schematic of the ELISA performed in the fabricated multistack is shown in Figure 6b the details of which are given in the Experimental Section (here, Cap Ab, capture antibody; Atg, antigen; Det Ab, detection antibody; Strp-Ag, streptavidin AgNP). While this is the case with the SPCE platform, directional GraPE and beaming GraSE presented 183-fold and 92-fold emission enhancements, respectively, with the maximum concentration of antigen, i.e., 2000 pg mL^{-1}. Upon reduction in the antigen concentration, the number of AgNPs generating the hot-spots dwindled, resulting in reduced emission enhancements. This was accompanied by a reduced number of nanogaps between the NPs and sensing platform as reported earlier.[48,64−66] This was in turn used to understand the interfacial interactions of the antigen and antibody and detection of IFN-γ. Parts c and d of Figure 6 display the calibration plots for the GraPE and GraSE detection platforms. While the linear fit observed for GraPE was in the range 1.95−1000 pg mL^{-1} (R = 0.988) with an 1.95 pg mL^{-1} limit of detection, the same for GraSE was observed to be in the range 31.25−1000 pg mL^{-1} (R = 0.989) with a 31.25 pg mL^{-1} limit of detection. The large linear range exhibited by the GraPE platform (compared to conventional ELISA and SPCE) is reasonable on account of the large coupling efficiency of the PMMA|GO multistack with the radiating dipoles. From an earlier section, we noted that the cavity environment generated by any NP results in higher emission enhancements in GraPE as compared to those of SPCE. Hence, the utility of GraSP engineering was demonstrated in biosensing by the dual benefits of GO plasmons and the solitons (of the multistack) presenting reliable, sensitive, and reproducible results with a much lower limit of detection in comparison to conventional ELISA and SPCE. Unlike the earlier reports where ELISA was established in a directional SPCE platform,[48,64,65] this report presents a convenient way for the collection of emission signal in the case of GraSE where the position of the detector is fixed. In this approach, we avoided the intricate labeling of biomolecules (such as antibodies) to fluorophores by adopting the well-established cavity architecture for signal collection, both in SPCE and GraSP. This label-free technique was achieved simply by directly spin-coating the radiating dipoles on the platform. Moreover, several advantages of GraSP engineering on account of wide optical window, directionality, reduced background noise, and polarization properties that were discussed in earlier sections of this report can be further improved and optimized for biosensing applications on the basis of specific requirements. Earlier reports validate the importance of the SPCE platform as an efficient framework for performing immunoassays even in optically dense matrices including blood samples.[64,65] Furthermore, it is informative to discuss the different methodologies that have been developed for the detection of IFN-γ and draw a comparative analysis with the technique developed in this work. From Table S2, we note that reports in the literature, in the past 10 years, utilized a variety of materials and techniques for both the qualitative and ultrasensitive detection of IFN-γ. These reports have been comprehensively summarized in Table S2 in terms of their limit of detection and linear sensing range along with key highlights. In light of these observations, it is worth mentioning that the proposed GraPE detection technology using the GO|PMMA multistack presents itself as a salient methodology and has demonstrated a better limit of detection compared to those of existing techniques. Further, the ability to integrate this in-house developed platform with a simple, rapid, low-cost spin-coating technique presents for near real-time point-of-care diagnostic applications in resource-limited settings. In this context, further experiments to understand the merits and demerits of the GraSP detection platform under different disease conditions are underway with the use of healthy and infected serum, blood, saliva, plasma, and urine samples. Of late, PMMA-based microfluidic devices[67] are being studied for sensing applications, and hence, we strongly believe that the GraSP platform could be used for monitoring human IFN-γ in biological samples using such PMMA multistack-based detection platforms.

CONCLUSIONS

In summary, this report presents a simple, user-friendly, cost-effective spin-coating technique to realize GraSP emission with soliton-aided MDM analogues and directional emission patterns on a conventional SPCE platform. The utilization of a 7 BLs multistack resulted in 35-fold emission enhancements, while a cavity environment generated with AgCDs supporting multiple hot-spots resulted in >900-fold fluorescence enhancements in the otherwise omnidirectional uncoupled FS emission. This report attempts to bring a directional emission characteristic of SPCE and GO-assisted soliton states onto a single metal-free and template-free GraPE platform. The deliberate use of RK configuration was essential to capture the beaming emission on account of soliton states. While SPCE aids in the coupling of only p-polarized light, GraSP engineering allows one to realize the coupling of both p- and s-polarized emission due to nonlinear and linear contributions.

The impacts of this study are threefold: (i) This approach could find applications in metal-free plasmonic sensor platforms with applications in optofluidic PMMA chip-based smart plasmonic devices. (ii) GO has already been extensively used for different sensing and light confinement technologies, which makes GraSP engineering an entirely new counterpart of SPCE technology. (iii) It holds great promise for the tunability and steering of fluorescence emission, resulting in reconfig-

https://doi.org/10.1021/acsami.1c01024
ACS Appl. Mater. Interfaces 2021, 13, 17046−17061

urable plasmonics at novel interfaces with new opportunities for biomedical point-of-care diagnostics. We envisage the immediate deployment of these low-cost, metal-free multistacks for bioanalytical, chemical, and forensic sensing applications. Doping individual layers of the multistack with different NPs would open a new arena of research in graphene oxide interfacial plasmonics. We strongly believe that this study presents a stepping stone to a plethora of exciting plasmonic architectures with doping of compositionally different multistacks containing analogous 2D nanomaterials (such as nitrides and carbides) to fully exploit their plasmonic and optical response.

EXPERIMENTAL SECTION

Chemicals. Pyrex microscopic slides vapor-deposited with Ag thin film (50 nm) were purchased from EMF corp. Rhodamine B (RhB), poly(methyl methacrylate) (PMMA), rhodamine 6G (Rh6G), polyvinyl alcohol (PVA), and Nd_2O_3 NRs were procured from Sigma-Aldrich. Intermetallics/SiO_2 NPs were obtained from Tata Chemicals Ltd. TiO_2 NPs were procured from US Research Nanomaterials, Inc. TiC, TiN, and TiCN were procured from Reinst, Nano Ventures. AgNPs (Turkevich method) and AuNPs were synthesized via well-established procedures.[2,6] PtNPs was obtained as a gratis sample. Invitrogen IFN γ human matched antibody pair "ELISA IFN-γ Cytoset" (Cat. # CHC1233), Life Technologies, was procured from Thermo Fisher Scientific. All the experimental solutions of the antibodies, antigen, and other reagents dilutions required for sandwich enzyme-linked immunosorbent assay (ELISA) were made using the recommended Invitrogen buffer kit for antibody pairs (Cat. # CNB0011) procured from Thermo Fisher Scientific. A F96 Maxisorp NUNC-Immuno plate (Cat. #442404) procured from Thermo Fisher Scientific was used for the conventional ELISA. Streptavidin-40 nm silver nanoparticles conjugate solution was procured from Cytodiagnostics (Cat. # SC-40-04).

GraSP Engineering Protocol. The multistack was prepared by spin-coating technology as reported earlier.[28,68] First, GO (0.5 mg/mL) was spin-coated on a glass slide at 9000 rpm for 60 s, to give a 0.9−1.1 nm thick GO.[68] This was followed by spin-coating PMMA (0.25g/mL) dissolved in $CHCl_3$.[28,69] This gave a PMMA thin film with a thickness of 460−480 nm. However, since GO was dissolved in Milli-Q water and PMMA in $CHCl_3$, spin-coating GO on PMMA did not help to obtain the required multistack due to repulsive interactions between polar and nonpolar entities. Hence, in order to successfully spin-coat GO on PMMA, the PMMA layer was subjected to corona treatment. This resulted in the dangling surface oxygen functional groups that aided in the bonding of GO that was immediately spin-coated on corona-treated PMMA. It must be noted that alterations in thickness, 450 nm PMMA layer with ±50 nm, did not result in any significant changes in the reflectance profile (Supporting Information). Also, a variation in the thickness of GO in the range 0.6−1.6 nm did not affect the MPR resonances. This procedure was taken forward for the preparation of the desired number of BLs. The engineered GraSP substrates [glass slides with BLs] were affixed to a hemicylindrical prism using an index matching fluid glycerol (1.47). This prism was mounted on a calibrated 360° rotating stage. All GraSP experiments were performed in reverse Kretchmann (RK) configuration.[29,30,34,35] A 5 mW, 532 nm c.w. laser excitation was incidented onto the engineered GraSP substrates, and plasmon-coupled emission was collected from the distal part of the prism using a 550 nm long wave pass (LWP) filter. An USB4000 fiber optic spectrometer connected to Ocean Optics SpectraSuite software was utilized for recording free space (FS), GraSE, and GraPE. A sheet polarizer was placed in between the prism and fiber optic collector in vertical and horizontal orientations to capture p- and s-polarized emission. The fluorescence emission enhancements were calculated as the ratio of GraSP emission intensity counts to FS emission intensity counts. The directionality of the angular emission was determined for all the samples, as reported earlier.[29,30,34,35]

Cavity Engineering Protocol. The blank for cavity interface was prepared by spin-coating dye doped polymer as a single layer on top of the multistack. The cavity is the infinitesimal nanogap between NPs and the fabricated multistack. This was prepared by spin-coating a blend of RhB and the NPs on top of the multistack as reported in our earlier publications.[29,30,34,35,51] In brief, NPs were admixed with emitter dipoles and spin-coated on top of the multistack at 3000 rpm for 60 s using PVA as a polymer matrix. This resulted in an overcoat of 30 nm thickness. The region between the NP and multistack, where the radiating dipoles are sandwiched, experiences augmented EM-field intensity. As a result, depending upon the plasmonic behavior of NPs to confine light to a cavity environment, tunable emission enhancements can be achieved.

FDTD and TFCalc Simulations. TFCalc solftware (Software Spectra) was used to carry out simulations on the basis of SPR theory and to validate observed emission angles. The theory of SPR and SPCE being complementary to each other suggests that regions of minimum reflectivity can give rise to enhancements in emission from a radiating dipole.[36] The parameters used as inputs during the simulations are as follows: n_s = 1.50 for PVA, n_{PMMA} = 1.49, n_{GO} = 2 + 0.3i, 1 mm BK7 glass (n_g = 1.518) corresponding to the wavelength maxima,[70] where n is the refractive index.

Lumerical's FDTD solutions, a commercially available software, were used for the simulation of the various hot-spots. The multistack structure was created with material and simulation properties available within the software. The conceptual schematic is presented in Figure S24. An in-built dipole source was used after matching its emission with that of RhB. The simulations were carried out at 0.1 nm resolution in 3D, and the resulting PFs were exported and correlated with enhancements obtained from the experiments. Figure S24 represents the cavity architecture that shows high electromagnetic field intensity at the gap between the nanomaterial and plasmonic thin film. This area is referred to as a hot-spot. When a dipole emitter is present in this hot-spot, the electromagnetic field experienced by the emitter is much higher when compared to that in the absence of the cavity. This variation was calculated as the Purcell factor (PF). In this work, we carried out FDTD simulations with various nanomaterials as part of the cavity and correlated their PF to the experimental outcome.

ELISA Protocol. The calibration concentrations of IFN-γ were measured using conventional sandwich ELISA (absorbance technique) as per the manufacturer's recommended protocol. The immuno microwell plate was coated with 100 μL/well of 2 μg/mL coating antibody solution and incubated at 4 °C for 18 h. The coating antibody solution was aspirated out, and the wells were washed once with 300 μL of washing buffer per well. Following the wash, the remnant liquid was removed by inverting and tapping the plate on an absorbent paper. The assay buffer (300 μL/well) was added and incubated at room temperature for 1 h for blocking the nonspecific sites of the capture antibody. Calculated concentrations (100 μL) of recombinant IFN-γ diluted serially in assay buffer (ranging from 2000 to 31.25 pg/mL) were pipetted into designated wells in triplicate. Immediately, 50 μL/well of the working detection antibody solution, 0.16 μg/mL, diluted in assay buffer was added and incubated at room temperature for 2 h with shaking at 700 rpm. The solutions were aspirated out, and the wells were washed five times with 300 μL of washing buffer per well. Following each wash, the remnant liquid was removed by inverting and tapping the plate on an absorbent paper. The working streptavidin-HRP solution (100 μL) prepared in assay buffer was pipetted into each of the well, followed by 30 min of incubation at room temperature with shaking at 700 rpm. The solutions were aspirated out, and the wells were washed five times with 300 μL of washing buffer per well. Following each wash, the remnant liquid was removed by inverting and tapping the plate on an absorbent paper. The TMB substrate solution (100 μL) was pipetted into each well, followed by 30 min of incubation at room temperature with shaking at 700 rpm. The stop solution (100 μL) was pipetted into each well. The absorbance was measured at 450 nm (reference absorbance at 650 nm) using a Varioskan LUX Multimode Microplate Reader (Thermo Fisher Scientific). A similar protocol was adopted

https://doi.org/10.1021/acsami.1c01024
ACS Appl. Mater. Interfaces 2021, 13, 17046−17061

for SPCE and GraSP platforms. Pyrex microscopic slides vapor-deposited with Ag thin film (50 nm) comprised the SPCE substrate. The 7 BLs of GO|PMMA fabricated atop pyrex microscopic slides comprised the GraSP emission substrate. Initially, 0.7 mg/mL PMMA in chloroform containing 1 mM Rh6G was spin-coated on top of SPCE and GraSP emission platforms to get a 5 nm thick polymer overcoat. The PMMA overcoats were corona-treated for 3 s just before coating the primary antibody so as to generate oxygen functionalities as described in preceding sections. The slides were coated with coating antibody solution to cover the surface of the slide (cut with dimensions 2 cm × 1 cm) and incubated at 4 °C for 18 h. The coating antibody solution was aspirated out, and the SPCE and GraSP substrates were washed once with washing buffer to remove the unbound coating antibody. Next, an assay buffer covering the surface was added and incubated at room temperature for 1 h for blocking the nonspecific binding sites. After the assay buffer was drained out of the slides, 80 μL of calculated concentrations of recombinant IFN-γ diluted serially in assay buffer (ranging from 2000 to 1.95 pg/mL) were pipetted onto the SPCE and GraSP substrates in triplicate. Immediately, 40 μL of working detection antibody solution, 0.16 μg/mL, diluted in assay buffer was added, and the substrates were incubated at room temperature for 2 h with shaking at 45 rpm. The solutions were aspirated out, and the substrates were washed thrice with washing buffer and drained of any remnant liquid. An 80 μL of working streptavidin-40 nm silver nanoparticles conjugate solution (prepared in assay buffer) was pipetted onto each substrate, followed by 30 min incubation at room temperature with shaking at 45 rpm. Solutions were aspirated out of the substrates, followed by three times wash using a washing buffer and a complete draining of remnant liquid.

■ ASSOCIATED CONTENT

Supporting Information

The Supporting Information is available free of charge at https://pubs.acs.org/doi/10.1021/acsami.1c01024.

Discussions of chemicals used, characterization details, additional explanation regarding Figures 1 and 3 of main manuscript, vibrational stretching bands of PMMA thin film, AFM characterization and analysis, five-fold purpose and motivation behind the research, detailed analysis of resonant dips in reflectivity, graphene oxide plasmon-coupled emission, dispersion diagrams and associated analysis, and distinctive properties of GraSP engineering with futuristic scope, tables of positions and assignment of prominent absorption bands in PMMA and comparison of recent techniques/strategies developed to detect IFN-γ with GraPE platform, and figures of AFM images, corresponding height profiles, reflectivity plots, EFI plots, reflectance profiles, emission spectra, angularity plots, wavelength vs angle dispersion diagram, frequency vs wave vector dispersion diagram, hybridized plasmon model, short range and long range coupling of analyte of interest from the multistack substrate, TEM and HRTEM images, SAED, XRD patterns, UV−vis absorbance spectra, GraPE and GraSE enhancements, calibration curves, schematic of the multistack structure, and cavity architecture showing high electromagnetic field intensity (PDF)

■ AUTHOR INFORMATION

Corresponding Authors

Venkatesh Srinivasan − *STAR Laboratory, Department of Chemistry, Sri Sathya Sai Institute of Higher Learning, Anantapur, Andhra Pradesh 515134, India;* orcid.org/0000-0002-4425-8260; Phone: +91-9573387852; Email: venkateshs@sssihl.edu.in

Sai Sathish Ramamurthy − *STAR Laboratory, Department of Chemistry, Sri Sathya Sai Institute of Higher Learning, Anantapur, Andhra Pradesh 515134, India;* orcid.org/0000-0001-9957-9259; Phone: +91-8790314405; Email: rsaisathish@sssihl.edu.in

Authors

Seemesh Bhaskar − *STAR Laboratory, Department of Chemistry, Sri Sathya Sai Institute of Higher Learning, Anantapur, Andhra Pradesh 515134, India;* orcid.org/0000-0003-2714-3776

Naga Sai Visweswar Kambhampati − *STAR Laboratory, Department of Chemistry, Sri Sathya Sai Institute of Higher Learning, Anantapur, Andhra Pradesh 515134, India*

K. M. Ganesh − *STAR Laboratory, Department of Chemistry, Sri Sathya Sai Institute of Higher Learning, Anantapur, Andhra Pradesh 515134, India*

Mahesh Sharma P − *STAR Laboratory, Department of Chemistry, Sri Sathya Sai Institute of Higher Learning, Anantapur, Andhra Pradesh 515134, India*

Complete contact information is available at: https://pubs.acs.org/10.1021/acsami.1c01024

Author Contributions

All authors have given approval to the final version of the manuscript.

Notes

The authors declare no competing financial interest.

■ ACKNOWLEDGMENTS

S.S.R., V.S., N.S.V.K., and S.B. acknowledge support from Tata Education and Development Trust [TEDT/MUM/HEA/SSSIHL/2017-2018/0069-RM-db], Prasanthi Trust, Inc. [22-06-2018], DST-Technology Development Program [IDP/MED/19/2016], Life Sciences Research Board (LSRB), DRDO - Defence Research and Development Organization [O/o DG/81/48222/LSRB-337/BTB/2018], and DST-Inspire Research Fellowship [IF180392], Govt. of India. S.B. and N.S.V.K. would like to thank Dr. S. Venketesh and Sri Sai Krishna S. B., Dept. of Biosciences, SSSIHL for study inputs and assistance in biosensing studies. S.B. would like to thank Dr. Shivakiran Bhaktha B. N. and Dr. Pratyusha Das, Dept. of Physics, IIT-Kharagpur for providing FESEM data and MATLAB simulations. S.B. would like to thank Dr. Shailesh Srivastava, Dept. of Physics, SSSIHL for study inputs. The authors specially acknowledge SSSIHL-CRIF for extending the usage of the required instrumentation facility.

■ DEDICATION

This year marks the 10th anniversary since the inception of the plasmonics lab at SSSIHL. At this juncture, we dedicate this work to Bhagawan Sri Sathya Sai Baba, Founder Chancellor, SSSIHL, to commemorate his yeoman service to humanity on the occasion of the 10th Sri Sathya Sai Aradhana Mahotsavam. As we bid 2020 goodbye, we also dedicate this research to all the first responders of the COVID-19 pandemic.

■ ABBREVIATIONS

GraSE, graphene oxide plasmon-coupled soliton emission; GraPE, graphene oxide plasmon-coupled emission; SPCE,

surface plasmon-coupled emission; PFs, Purcell factors; NPs, nanoparticles; MEF, metal enhanced fluorescence; MD, metal−dielectric; MDM, metal−dielectric−metal; HRI, high refractive index; LRI, low refractive index; NRs, nanorods; RK, reverse Kretchmann; KR, Kretschmann-Raether; MPR, multistack plasmon resonance; 1DPCs, one-dimensional photonic crystal; EM, electromagnetic; SPPs, surface plasmon polaritons; IFN-γ, interferon γ; GO, graphene oxide; PMMA, polymethyl methacrylate; EFI, electric field intensity, FDTD, finite-difference time-domain; SLGO, single layer graphene oxide; BGCE, Bragg-grating coupled emission; BSW, Bloch surface wave; IOM, internal optical mode; FESEM, field emission scanning electron microscope; TM, transverse magnetic; TE, transverse electric; SPR, surface plasmon resonance; HRTEM, high-resolution transmission electron microscope; SAED, selected area electron diffraction; AFM, atomic force microscopy; PVA, poly(vinyl alcohol); XRD, X-ray diffraction; FTIR, Fourier transform infrared; DOS, density of states; TFCalc, thin film calculations; TSCE, Tamm state-coupled emission, ICSD, Inorganic Crystal Structure Database; ELISA, enzyme-linked immunosorbent assay; Rh6G, rhodamine 6G

REFERENCES

(1) Yu, H.; Peng, Y.; Yang, Y.; Li, Z. Y. Plasmon-Enhanced Light-Matter Interactions and Applications. *npj Comput. Mater.* **2019**, *5*, 45.

(2) Jiang, N.; Zhuo, X.; Wang, J. Active Plasmonics: Principles, Structures, and Applications. *Chem. Rev.* **2018**, *118*, 3054−3099.

(3) Jahani, S.; Jacob, Z. All-Dielectric Metamaterials. *Nat. Nanotechnol.* **2016**, *11*, 23.

(4) Koppens, F. H.; Chang, D. E.; García de Abajo, F. J. Graphene Plasmonics: A Platform for Strong Light-Matter Interactions. *Nano Lett.* **2011**, *11*, 3370−3377.

(5) Koenderink, A. F.; Alu, A.; Polman, A. Nanophotonics: Shrinking Light-Based Technology. *Science* **2015**, *348*, 516−521.

(6) Naik, G. V.; Shalaev, V. M.; Boltasseva, A. Alternative Plasmonic Materials: Beyond Gold and Silver. *Adv. Mater.* **2013**, *25*, 3264−3294.

(7) Sunku, S. S.; Ni, G.; Jiang, B. Y.; Yoo, H.; Sternbach, A.; McLeod, A. S.; Stauber, T.; Xiong, L.; Taniguchi, T.; Watanabe, K.; Kim, P.; et al. Photonic Crystals for Nano-Light in Moiré Graphene Superlattices. *Science* **2018**, *362*, 1153−1156.

(8) Gu, T.; Andryieuski, A.; Hao, Y.; Li, Y.; Hone, J.; Wong, C. W.; Lavrinenko, A.; Low, T.; Heinz, T. F. Photonic and Plasmonic Guided Modes in Graphene-Silicon Photonic Crystals. *ACS Photonics* **2015**, *2*, 1552−1558.

(9) Cox, J. D.; De Abajo, F. J. G. Electrically Tunable Nonlinear Plasmonics in Graphene Nanoislands. *Nat. Commun.* **2014**, *5*, 5725.

(10) Garcia de Abajo, F. J. Graphene Plasmonics: Challenges and Opportunities. *ACS Photonics* **2014**, *1*, 135−152.

(11) Fang, Z.; Wang, Y.; Schlather, A. E.; Liu, Z.; Ajayan, P. M.; García de Abajo, F. J.; Nordlander, P.; Zhu, X.; Halas, N. J. Active Tunable Absorption Enhancement with Graphene Nanodisk Arrays. *Nano Lett.* **2014**, *14*, 299−304.

(12) Ishikawa, A.; Tanaka, T. Plasmon Hybridization in Graphene Metamaterials. *Appl. Phys. Lett.* **2013**, *102*, 253110.

(13) Rodrigo, D.; Tittl, A.; Limaj, O.; De Abajo, F. J. G.; Pruneri, V.; Altug, H. Double-Layer Graphene for Enhanced Tunable Infrared Plasmonics. *Light: Sci. Appl.* **2017**, *6*, e16277.

(14) Yan, H.; Xia, F.; Li, Z.; Avouris, P. Plasmonics of Coupled Graphene Micro-Structures. *New J. Phys.* **2012**, *14*, 125001.

(15) Gumbs, G.; Iurov, A.; Wu, J. Y.; Lin, M. F.; Fekete, P. Plasmon Excitations of Multi-Layer Graphene on a Conducting Substrate. *Sci. Rep.* **2016**, *6*, 21063.

(16) Smirnova, D. A.; Shadrivov, I. V.; Smirnov, A. I.; Kivshar, Y. S. Dissipative Plasmon-Solitons in Multilayer Graphene. *Laser Photonics Rev.* **2014**, *8*, 291−296.

(17) Bludov, Y. V.; Smirnova, D. A.; Kivshar, Y. S.; Peres, N. M.; Vasilevskiy, M. I. Discrete Solitons in Graphene Metamaterials. *Phys. Rev. B: Condens. Matter Mater. Phys.* **2015**, *91*, 045424.

(18) Iorsh, I. V.; Mukhin, I. S.; Shadrivov, I. V.; Belov, P. A.; Kivshar, Y. S. Hyperbolic Metamaterials based on Multilayer Graphene Structures. *Phys. Rev. B: Condens. Matter Mater. Phys.* **2013**, *87*, 075416.

(19) Avouris, P.; Dimitrakopoulos, C. Graphene: Synthesis and Applications. *Mater. Today* **2012**, *15*, 86−97.

(20) Dreyer, D. R.; Park, S.; Bielawski, C. W.; Ruoff, R. S. The Chemistry of Graphene Oxide. *Chem. Soc. Rev.* **2010**, *39*, 228−240.

(21) Zhen, C.; Wu, T.; Chen, R.; Wang, L.; Liu, G.; Cheng, H. M. Strategies for Modifying TiO_2 Based Electron Transport Layers to Boost Perovskite Solar Cells. *ACS Sustainable Chem. Eng.* **2019**, *7*, 4586−4618.

(22) Lin, C.; Jiang, Y.; Tao, C. A.; Yin, X.; Lan, Y.; Wang, C.; Wang, S.; Liu, X.; Li, G. Electrothermally Driven Fluorescence Switching by Liquid Crystal Elastomers based on Dimensional Photonic Crystals. *ACS Appl. Mater. Interfaces* **2017**, *9*, 11770−11779.

(23) Badugu, R.; Nowaczyk, K.; Descrovi, E.; Lakowicz, J. R. Radiative Decay Engineering 6: Fluorescence on One-Dimensional Photonic Crystals. *Anal. Biochem.* **2013**, *442*, 83−96.

(24) Badugu, R.; Descrovi, E.; Lakowicz, J. R. Radiative decay engineering 7: Tamm State-Coupled Emission using a Hybrid Plasmonic-Photonic Structure. *Anal. Biochem.* **2014**, *445*, 1−13.

(25) Dutta Choudhury, S.; Badugu, R.; Nowaczyk, K.; Ray, K.; Lakowicz, J. R. Tuning Fluorescence Direction with Plasmonic Metal-Dielectric-Metal Substrates. *J. Phys. Chem. Lett.* **2013**, *4*, 227−232.

(26) Fu, B.; Li, J.; Cao, Z.; Popa, D. Bound States of Solitons in a Harmonic Graphene-Mode-Locked Fiber Laser. *Photonics Res.* **2019**, *7*, 116−120.

(27) Gubaydullin, A. R.; Symonds, C.; Bellessa, J.; Ivanov, K. A.; Kolykhalova, E. D.; Sasin, M. E.; Lemaitre, A.; Senellart, P.; Pozina, G.; Kaliteevski, M. A. Enhancement of Spontaneous Emission in Tamm Plasmon Structures. *Sci. Rep.* **2017**, *7*, 9014.

(28) Sreekanth, K. V.; Zeng, S.; Shang, J.; Yong, K. T.; Yu, T. Excitation of Surface Electromagnetic Waves in a Graphene-based Bragg Grating. *Sci. Rep.* **2012**, *2*, 737.

(29) Bhaskar, S.; Moronshing, M.; Srinivasan, V.; Badiya, P. K.; Subramaniam, C.; Ramamurthy, S. S. Silver Soret Nanoparticles for Femtomolar Sensing of Glutathione in a Surface Plasmon-Coupled Emission Platform. *ACS Appl. Nano Mater.* **2020**, *3*, 4329−4341.

(30) Bhaskar, S.; Kowshik, N. C. S.; Chandran, S. P.; Ramamurthy, S. S. Femtomolar Detection of Spermidine Using Au Decorated SiO_2 Nanohybrid on Plasmon-Coupled Extended Cavity Nanointerface: A Smartphone-Based Fluorescence Dequenching Approach. *Langmuir* **2020**, *36*, 2865−2876.

(31) Gullans, M.; Chang, D. E.; Koppens, F. H. L.; de Abajo, F. G.; Lukin, M. D. Single-Photon Nonlinear Optics with Graphene Plasmons. *Phys. Rev. Lett.* **2013**, *111*, 247401.

(32) Ju, L.; Geng, B.; Horng, J.; Girit, C.; Martin, M.; Hao, Z.; Bechtel, H. A.; Liang, X.; Zettl, A.; Shen, Y. R.; Wang, F. Graphene Plasmonics for Tunable Terahertz Metamaterials. *Nat. Nanotechnol.* **2011**, *6*, 630.

(33) Yan, H.; Li, X.; Chandra, B.; Tulevski, G.; Wu, Y.; Freitag, M.; Zhu, W.; Avouris, P.; Xia, F. Tunable Infrared Plasmonic Devices using Graphene/Insulator Stacks. *Nat. Nanotechnol.* **2012**, *7*, 330.

(34) Bhaskar, S.; Das, P.; Srinivasan, V.; Bhaktha BN, S.; Ramamurthy, S. S. Bloch Surface Waves and Internal Optical Modes-Driven Photonic Crystal-Coupled Emission Platform for Femtomolar Detection of Aluminum Ions. *J. Phys. Chem. C* **2020**, *124*, 7341−7352.

(35) Bhaskar, S.; Patra, R.; Kowshik, N.C. S.S.; Ganesh, K.M.; Srinivasan, V.; Chandran S, P.; Ramamurthy, S. S. Nanostructure Effect on Quenching and Dequenching of Quantum Emitters on Surface Plasmon-Coupled Interface: A Comparative Analysis using Gold Nanospheres and Nanostars. *Phys. E (Amsterdam, Neth.)* **2020**, *124*, 114276.

https://doi.org/10.1021/acsami.1c01024
ACS Appl. Mater. Interfaces 2021, 13, 17046−17061

(36) Lakowicz, J. R. Radiative decay engineering 3. Surface Plasmon-Coupled Directional Emission. *Anal. Biochem.* **2004**, *324*, 153−169.
(37) Wilson, N. R.; Pandey, P. A.; Beanland, R.; Young, R. J.; Kinloch, I. A.; Gong, L.; Liu, Z.; Suenaga, K.; Rourke, J. P.; York, S. J.; Sloan, J. Graphene Oxide: Structural Analysis and Application as a Highly Transparent Support for Electron Microscopy. *ACS Nano* **2009**, *3*, 2547−2556.
(38) Li, S. S.; Tu, K. H.; Lin, C. C.; Chen, C. W.; Chhowalla, M. Solution-Processable Graphene Oxide as an Efficient Hole Transport Layer in Polymer Solar Cells. *ACS Nano* **2010**, *4*, 3169−3174.
(39) Saxena, S.; Tyson, T. A.; Shukla, S.; Negusse, E.; Chen, H.; Bai, J. Investigation of Structural and Electronic Properties of Graphene Oxide. *Appl. Phys. Lett.* **2011**, *99*, 013104.
(40) Yin, F.; Wu, S.; Wang, Y.; Wu, L.; Yuan, P.; Wang, X. Self-Assembly of Mildly Reduced Graphene Oxide Monolayer for Enhanced Raman Scattering. *J. Solid State Chem.* **2016**, *237*, 57−63.
(41) Huang, H. H.; De Silva, K. K. H.; Kumara, G. R. A.; Yoshimura, M. Structural Evolution of Hydrothermally Derived Reduced Graphene Oxide. *Sci. Rep.* **2018**, *8*, 6849.
(42) Dimiev, A. M.; Eigler, S. *Graphene oxide: fundamentals and applications*; John Wiley & Sons, 2016.
(43) Zhang, C.; Dabbs, D. M.; Liu, L. M.; Aksay, I. A.; Car, R.; Selloni, A. Combined Effects of Functional Groups, Lattice Defects, and Edges in the Infrared Spectra of Graphene Oxide. *J. Phys. Chem. C* **2015**, *119*, 18167−18176.
(44) Erickson, K.; Erni, R.; Lee, Z.; Alem, N.; Gannett, W.; Zettl, A. Determination of the Local Chemical Structure of Graphene Oxide and Reduced Graphene Oxide. *Adv. Mater.* **2010**, *22*, 4467−4472.
(45) Wang, R.; Xia, H.; Zhang, D.; Chen, J.; Zhu, L.; Wang, Y.; Yang, E.; Zang, T.; Wen, X.; Zou, G.; Wang, P.; et al. Bloch Surface Waves Confined in One Dimension with a Single Polymeric Nanofibre. *Nat. Commun.* **2017**, *8*, 14330.
(46) Uddin, S. Z.; Tanvir, M. R.; Talukder, M. A. A Proposal and a Theoretical Analysis of an Enhanced Surface Plasmon Coupled Emission Structure for Single Molecule Detection. *J. Appl. Phys.* **2016**, *119*, 204701.
(47) Tran, N. H. T.; Trinh, K. T. L.; Lee, J. H.; Yoon, W. J.; Ju, H. Reproducible Enhancement of Fluorescence by Bimetal Mediated Surface Plasmon Coupled Emission for Highly Sensitive Quantitative Diagnosis of Double-Stranded DNA. *Small* **2018**, *14*, 1801385.
(48) Cao, S. H.; Cai, W. P.; Liu, Q.; Xie, K. X.; Weng, Y. H.; Huo, S. X.; Tian, Z. Q.; Li, Y. Q Label-Free Aptasensor based on Ultrathin-Linker-Mediated Hot-Spot Assembly to Induce Strong Directional Fluorescence. *J. Am. Chem. Soc.* **2014**, *136*, 6802−6805.
(49) Kim, H.; Ge, J.; Kim, J.; Choi, S. E.; Lee, H.; Lee, H.; Park, W.; Yin, Y.; Kwon, S. Structural Colour Printing using a Magnetically Tunable and Lithographically Fixable Photonic Crystal. *Nat. Photonics* **2009**, *3*, 534.
(50) Boehm, H. P.; Setton, R.; Stumpp, E. Nomenclature and Terminology of Graphite Intercalation Compounds (IUPAC Recommendations 1994). *Pure Appl. Chem.* **1994**, *66*, 1893−1901.
(51) Venkatesh, S.; Badiya, P. K.; Ramamurthy, S. S. Low-Dimensional Carbon Spacers in Surface Plasmon-Coupled Emission with Femtomolar Sensitivity and 1000-fold Fluorescence Enhancements. *Chem. Commun.* **2015**, *51*, 7809−7811.
(52) Förg, M.; Colombier, L.; Patel, R. K.; Lindlau, J.; Mohite, A. D.; Yamaguchi, H.; Glazov, M. M.; Hunger, D.; Högele, A. Cavity-Control of Interlayer Excitons in Van Der Waals Heterostructures. *Nat. Commun.* **2019**, *10*, 3697.
(53) Arathi, P. J.; Bhaskar, S.; Reddy, R. K.; Kumar, S. P.; Ramanathan, V. Disulphide linkage: To get Cleaved or not? Bulk and Nano Copper based SERS of Cystine. *Spectrochim. Acta, Part A* **2018**, *196*, 229−232.
(54) Arathi, P. J.; Bhaskar, S.; Reddy, R. K.; Kumar, S. P.; Ramanathan, V. The Photocatalytic Role of Electrodeposited Copper on Pencil Graphite. *Phys. Chem. Chem. Phys.* **2018**, *20*, 3430−3432.
(55) Bhaskar, S.; Ramamurthy, S. S. Mobile Phone-Based Picomolar Detection of Tannic Acid on Nd_2O_3 Nanorod-Metal Thin-Film Interfaces. *ACS Appl. Nano Mater.* **2019**, *2*, 4613−4625.
(56) Bhaskar, S.; Singh, A. K.; Das, P.; Jana, P.; Kanvah, S.; Bhaktha BN, S.; Ramamurthy, S. S. Superior Resonant Nanocavities Engineering on the Photonic Crystal-Coupled Emission Platform for the Detection of Femtomolar Iodide and Zeptomolar Cortisol. *ACS Appl. Mater. Interfaces* **2020**, *12*, 34323−34336.
(57) Kelchtermans, H.; Billiau, A.; Matthys, P. How Interferon-γ keeps Autoimmune Diseases in Check. *Trends Immunol.* **2008**, *29*, 479−486.
(58) Ivashkiv, L. B. IFNγ: Signalling, Epigenetics and Roles in Immunity, Metabolism, Disease and Cancer Immunotherapy. *Nat. Rev. Immunol.* **2018**, *18*, 545−558.
(59) Kak, G.; Raza, M.; Tiwari, B. K. Interferon-Gamma (IFN-γ): Exploring its Implications in Infectious Diseases. *Biomol. Concepts* **2018**, *9*, 64−79.
(60) Alspach, E.; Lussier, D. M.; Schreiber, R. D. Interferon γ and its Important Roles in Promoting and Inhibiting Spontaneous and Therapeutic Cancer Immunity. *Cold Spring Harb. Perspect. Biol.* **2019**, *11*, 028480.
(61) Zhang, F.; Deng, F.; Liu, G. J.; Middleton, R.; Inglis, D. W.; Anwer, A.; Wang, S.; Liu, G. IFN-γ-Induced Signal-On Fluorescence Aptasensors: from Hybridization Chain Reaction Amplification to 3D Optical Fiber Sensing Interface Towards a Deployable Device for Cytokine Sensing. *Mol. Syst. Des. Eng.* **2019**, *4*, 872−881.
(62) Ding, S.; Mosher, C.; Lee, X. Y.; Das, S. R.; Cargill, A. A.; Tang, X.; Chen, B.; McLamore, E. S.; Gomes, C.; Hostetter, J. M.; Claussen, J. C. Rapid and Label-Free Detection of Interferon Gamma via an Electrochemical Aptasensor Comprising a Ternary Surface Monolayer on a Gold Interdigitated Electrode Array. *ACS sensors* **2017**, *2*, 210−217.
(63) Desem, N.; Jones, S. L. Development of a Human Gamma Interferon Enzyme Immunoassay and Comparison with Tuberculin Skin Testing for Detection of Mycobacterium Tuberculosis Infection. *Clin. Diagn. Lab. Immunol.* **1998**, *5*, 531−536.
(64) Matveeva, E.; Gryczynski, Z.; Gryczynski, I.; Malicka, J.; Lakowicz, J. R. Myoglobin Immunoassay Utilizing Directional Surface Plasmon-Coupled Emission. *Anal. Chem.* **2004**, *76*, 6287−6292.
(65) Cao, S. H.; Cai, W. P.; Liu, Q.; Xie, K. X.; Weng, Y. H.; Li, Y. Q. Turning on Fluorescence by Plasmonic Assembly with Large Tunable Spacing: A New Observation and its Biosensing Application. *Chem. Commun.* **2014**, *50*, 518−520.
(66) Moronshing, M.; Bhaskar, S.; Mondal, S.; Ramamurthy, S. S.; Subramaniam, C. Surface-Enhanced Raman Scattering Platform Operating Over Wide Ph Range with Minimal Chemical Enhancement Effects: Test Case of Tyrosine. *J. Raman Spectrosc.* **2019**, *50*, 826−836.
(67) Matellan, C.; Armando, E. Cost-Effective Rapid Prototyping and Assembly of Poly (Methyl Methacrylate) Microfluidic Devices. *Sci. Rep.* **2018**, *8*, 6971.
(68) Yamaguchi, H.; Eda, G.; Mattevi, C.; Kim, H.; Chhowalla, M. Highly Uniform 300 mm Wafer-Scale Deposition of Single and Multilayered Chemically derived Graphene Thin Films. *ACS Nano* **2010**, *4*, 524−528.
(69) Walsh, C. B.; Franses, E. I. Ultrathin PMMA Films Spin-Coated from Toluene Solutions. *Thin Solid Films* **2003**, *429*, 71−76.
(70) Jung, I.; Pelton, M.; Piner, R.; Dikin, D. A.; Stankovich, S.; Watcharotone, S.; Hausner, M.; Ruoff, R. S. Simple Approach for High-Contrast Optical Imaging and Characterization of Graphene-based Sheets. *Nano Lett.* **2007**, *7*, 3569−3575.

https://doi.org/10.1021/acsami.1c01024
ACS Appl. Mater. Interfaces 2021, 13, 17046−17061